A phase-field model of two-phase Hele-Shaw flow

Luis Cueto-Felgueroso[1,2]†, **Ruben Juanes**[1]

[1]Department of Civil and Environmental Engineering,
Massachusetts Institute of Technology, Cambridge, USA
[2]Department of Civil Engineering: Hydraulics, Energy and the Environment,
Universidad Politécnica de Madrid, Madrid, Spain

We propose a continuum model of two-phase flow in a Hele-Shaw cell. The model describes the multiphase, three-dimensional flow in the cell gap using gap-averaged quantities such as fluid saturations and Darcy fluxes. Viscous and capillary coupling between the fluids in the gap leads to a nonlinear fractional flow function. Capillarity and wetting phenomena are modeled within a phase-field framework, designing a heuristic free energy functional that induces phase segregation at equilibrium. We test the model through the simulation of bubbles and viscously-unstable displacements (viscous fingering). We analyze the model's rich behavior as a function of capillary number, viscosity contrast and cell geometry. Including the effect of wetting films on the two-phase flow dynamics opens the door to exploring, with a simple, two-dimensional model, the impact of wetting and flow rate on the performance of microfluidic devices and geologic flows through fractures.

---

1. Introduction

The flow of immiscible fluids in the thin gap between two parallel plates—a Hele-Shaw cell—has been the focus of vast experimental, theoretical and modeling efforts over the past five decades (e.g Saffman & Taylor 1958*a*; Bensimon *et al.* 1986; Homsy 1987; McCloud & Maher 1995*a*; Casademunt 2004). This flow geometry is directly relevant for a number of applications, from microfluidics (Baroud *et al.* 2010; Dangla *et al.* 2011), to flow in fractured reservoirs (Persoff & Pruess 1995; Glass *et al.* 2001). In addition to its direct relevance, Hele-Shaw flow has also been used as an analogue system to understand flow in complex porous media (Homsy 1987), and some theoretical aspects of pattern formation in nonlinear systems (Casademunt 2004). The two flow scenarios that have been thoroughly investigated experimentally and theoretically are the motion and interaction of bubbles, and the viscously-unstable displacement of one fluid by another.

The motion of bubbles and droplets in a Hele-Shaw cell is a classical problem in fluid mechanics (Eck & Siekmann 1978; Park & Homsy 1984; Tanveer 1986; Maxworthy 1986; Kopf-Sill & Homsy 1988*a*; Meiburg 1989; Maruvada & Park 1996), which is receiving renewed attention due to its role in microfluidic applications (Baroud *et al.* 2010; Dangla *et al.* 2011). Experimental studies have shown a wealth of droplet shapes and flow regimes (Eck & Siekmann 1978; Maxworthy 1986; Kopf-Sill & Homsy 1988*a*; Maruvada & Park 1996), but a comprehensive theoretical explanation for the pattern

---

† Email address for correspondence: lcueto@mit.edu

selection mechanisms remains elusive (Park & Homsy 1984; Tanveer 1986). The flow set-up is simple: a volume of a fluid, surrounded by another viscous fluid, translates and distorts due to the constant flow-rate injection of the ambient fluid. The key questions then are what shape and velocity will the bubble adopt depending on the different system parameters, and whether the bubble will undergo breakup instabilities.

The instability of driven fronts in two-phase flow when the invading fluid is less viscous than the defending fluid is a classical problem in nonlinear pattern formation (Saffman & Taylor 1958b; Park & Homsy 1984, 1985; Homsy 1987; Kopf-Sill & Homsy 1988b). Viscous fingering impacts the displacement efficiency in multiphase flow through porous media, due to channeling and the subsequent creation of preferential flow paths. Because of these preferential paths, the sweep efficiency can be significantly reduced in the presence of fingering instabilities. Classical reviews on the subject can be found in Bensimon *et al.* (1986); Homsy (1987) and in McCloud & Maher (1995a). For isotropic cells and Newtonian fluids, detailed experimental observations and theoretical analysis go back to Saffman & Taylor (1958a). Other classical experiments include Paterson (1981); Park *et al.* (1984); Park & Homsy (1985); Maher (1985); Ben-Jacob *et al.* (1986); Tabeling *et al.* (1987); Kopf-Sill & Homsy (1988b); Arnéodo *et al.* (1989); Ben-Jacob & Garik (1990). These early experiments already show a rich phase diagram of displacement morphologies depending on viscosity contrast between the invading and defending fluids, and on the relative balance between viscous, capillary and gravitational forces. More recent studies include Carrillo *et al.* (1996, 1999); Lajeunesse & Couder (2000); Carrillo *et al.* (2000); Moore *et al.* (2002); Alvarez-Lacalle *et al.* (2004a); Miranda & Alvarez-Lacalle (2005); Alvarez-Lacalle *et al.* (2006). Variations in the Hele-Shaw geometry to account for variations in the gap width were considered in Zhao *et al.* (1992, 1993); Al-Housseiny *et al.* (2012), who introduce a gradient in the cell gap, and anisotropic cells were considered in McCloud & Maher (1995b); Decker *et al.* (1999); Banpurkar *et al.* (2000); Honda *et al.* (2006). Recently, there has been increased interest in flow control of the instability Li *et al.* (2009); Al-Housseiny *et al.* (2012), and complex fluid rheologies Buka *et al.* (1986, 1987); Lemaire *et al.* (1991); Zhao & Maher (1993); Park & Durian (1994); Corvera-Poiré & Amar (1998); Kawaguchi *et al.* (1999); Vlad & Maher (2000); Lindner *et al.* (2000a,b); Kawaguchi *et al.* (2001); Yamamoto *et al.* (2001); Lindner *et al.* (2002); Kawaguchi *et al.* (2004); Nagatsu *et al.* (2007). A large body of literature exists that addresses important theoretical aspects of the Saffman-Taylor instability, from pattern selection mechanisms to the stability of single-finger solutions and the effect of surface tension and wetting conditions (McLean & Saffman 1981; Park & Homsy 1984; Combescot *et al.* 1986; Howison 1986; Sarkar 1990; Weinstein *et al.* 1990; Casademunt & Jasnow 1991; Siegel *et al.* 1996; Siegel & Tanveer 1996; Somfai *et al.* 1999; Casademunt & Magdaleno 2000; Tanveer 2000; Ceniceros & Villalobos 2002; Alvarez-Lacalle *et al.* 2004b; Dias & Miranda 2013; Anjos & Miranda 2013; Nagel & Gallaire 2013).

The first sharp-interface simulations of fingering in Hele-Shaw cells were presented by Tryggvason & Aref (1983), with results that are qualitatively similar to the experiments of Maher (1985). Other early simulations using boundary integral methods are Degregoria & Schwartz (1986); Meiburg & Homsy (1988); Meiburg (1989); Park & Homsy (1985); a review of these early simulation methods was presented by Whitaker (1994). An important series of simulations based on boundary element methods was developed in Hou *et al.* (1994, 1997, 2001); Li *et al.* (2007, 2009). A similar approach is used by Almgren *et al.* (1993); Kondic *et al.* (1996); Shelley *et al.* (1997); Kondic *et al.* (1998); Fast *et al.* (2001); Fast & Shelley (2004), and by Sarkar & Jasnow (1989). In Alvarez-Lacalle *et al.* (2006) the authors apply one of the above boundary integral methods, imposing a boundary condition at the interface that models a preexisting wetting film.

Diffuse-interface theories of multiphase flow have recently emerged as promising tools to understand and simulate complex processes involving the simultaneous flow of two or more immiscible fluid phases (Anderson *et al.* 1998). These models originated in the materials science community, describing phase separation through the evolution of an order parameter—or ''phase field''—that defines a smooth transition between two phases (Cahn & Hilliard 1958; Cahn 1961). An overview of the application of phase-field modeling in condensed-matter physics can be found in Emmerich (2008). The fundamental idea of tracking and properly capturing interface dynamics thorugh phase-field theories has been subsequently generalized and adapted to mulitphase fluid flow scenarios. While variational or thermodynamic theories are perhaps the most common theorerical framework to rigorously derive these models (Antanovskii 1995; Jasnow & Viñals 1996; Lowengrub & Truskinovsky 1998; Anderson *et al.* 1998; Jacqmin 1999; Boyer 2002; Badalassi *et al.* 2003; Yue *et al.* 2004; Kim 2005; Ding *et al.* 2007; Lamorguese & Mauri 2008), diffuse-interface theories have been obtained from averaging microscale interactions (Sun & Beckermann 2004, 2007), or rationalized as a microforce balance (Gurtin 1994). The common goal in these approaches is to formulate thermodynamically consistent stress tensors and mesoscale balance laws, including the impact of surface tension on the momentum balance, as well as properly tracking interfacial dynamics (Lowengrub & Truskinovsky 1998).

Several phase-field or diffuse-interface models of Hele-Shaw flow have been proposed, expressing different modeling assumptions and theoretical approaches. These models are typically constructed either as particular versions of general multiphase flow theories to the lubrication-type flow in Hele-Shaw cells, or as continuum approximations to the 2D free-boundary problem. The model of Lee *et al.* (2002*a*,*b*), which is based on the thermodynamic theory for multiphase quasi-incompressible mixtures developed by Lowengrub & Truskinovsky (1998), uses a conserved order parameter (a concentration field) to describe the interface dynamics, and Darcy flow based on a mixture velocity. This Hele-Shaw-Cahn-Hilliard model has been recently used to study flow in rotating Hele-Shaw cells (Chen *et al.* 2011). The model by Sun & Beckermann (2008), based on the diffuse-interface theory developed by the same authors in a series of previous papers (Sun & Beckermann 2004, 2007), arises from averaging the microscale interface dynamics and uses a non-conserved order parameter to maintain the interface thickness. In some applications the interface dynamics may be described by a single Cahn-Hilliard equation, stressing the gradient-type nature of Hele-Shaw flows (Hernández-Machado *et al.* 2003; Glasner 2003; Lu *et al.* 2007). Folch *et al.* (1999*a*,*b*) proposed a phase-field model of two-phase Hele-Shaw flow with arbitrary viscosity contrast between the fluids. The model reduces to two evolution equations for the stream function and the phase field, converges to the sharp-interface 2D problem, and captures the multi-finger dynamics in viscous fingering. Phase-field models of Hele-Shaw flow for fluids with complex rheology have also been developed, for example (Nguyen *et al.* 2010) developed a phase-field model to study viscous fingering of shear-thinning fluids.

Here, we present a diffuse-interface model of two-phase flow in a Hele-Shaw cell. This model builds on our previous work on two-phase flow in a capillary tube (Cueto-Felgueroso & Juanes 2012). The main differentiating factor of our model in the vast literature of Hele-Shaw flow modeling is its ability to capture three-dimensional effects in a gap-averaged, Darcy-type formulation. The essential requirements to achieve this goal are the ability to capture the viscous and capillary coupling between fluids in the gap, and the impact of capillarity and wetting in the equilibrium of the two-phase system. The first key ingredient of our model is a non-convex fractional flow formulation that arises from the use of Darcy's law generalized to multiphase systems. This approach

has been traditionally used in the modeling of multiphase flow through porous media. The second ingredient is its behavior at equilibrium. We derive the capillary flow potentials from a free energy functional that induces fluid segregation in the absence of flow (Cahn & Hilliard 1958; Cueto-Felgueroso & Juanes 2012). Thus, equilibrium solutions are non-spreading, static bubbles within an ambient fluid. Under pressure-driven flow, the solutions involve the formation of non-classical shocks, which result in rich dynamic behavior. This novel feature captures the dependence of the thickness of wetting films left attached to the cell walls on the capillary number, in agreement with experimental observations. We test the properties of the model through one– and two–dimensional numerical solutions of the proposed model, and elucidate the displacement patterns for constant flow–rate and constant–volume injection. We analyze the existence and structure of the traveling wave solutions to our model, which provides important insight into the existence and structure of traveling bubbles and non–classical shock solutions.

Our model aims at capturing the 3D viscous and capillary coupling between fluids in the cell gap, in the context of a 2D, gap-averaged formulation. This goal is somehow different from the classical problem of approximating the 2D sharp-interface problem. The primary variables in our formulation, the fluid volume fractions, can be understood as phase fields, because they are used to represent the idea that either fluid may fully occupy the cell gap. As fluid volume fractions, fluid saturations have a direct physical interpretation, rather than being ad-hoc or auxiliary variables defining a smooth transition between two phases. Our model equations do not attempt to smooth a sharp-interface problem either. We should therefore note that we are using the idea of phase-field modeling in a generalized or loose sense. We have chosen to adopt the terminology of phase-field modeling, because we rely on a variational-type derivation of the flow potentials, in the spirit of phase–field and diffuse–interface models.

2. Mathematical model

2.1. *Darcy formulation of two-phase Hele-Shaw flow*

We consider incompressible, isothermal two-phase flow in a Hele-Shaw cell, driven by imposed pressure gradients and capillary forces. The evolution of fluid saturations can be expressed as conservation of mass of the two fluids:

$$\frac{\partial(b\rho_g S_g)}{\partial t} + \nabla \cdot (b\rho_g \mathbf{u}_g) = 0, \tag{2.1}$$

$$\frac{\partial(b\rho_w S_w)}{\partial t} + \nabla \cdot (b\rho_w \mathbf{u}_w) = 0. \tag{2.2}$$

For convenience, we refer to the two fluids as gas (subscript g) and water (subscript w), although their physical properties are general. Furthermore, we will assume that the gas is the non-wetting phase, and the water phase is the wetting phase. The saturation, S_α, of fluid phase $\alpha = g, w$, is the fraction of the gap that is occupied by that fluid. The width of the gap is b, the fluid densities are ρ_α, and $\mathbf{u}_\alpha$ is the volumetric flux of phase α. We adopt a Darcy formulation for the volumetric fluxes, where Darcy's law is generalized to multiphase systems (Bear 1972)

$$\mathbf{u}_g = -\lambda_g \nabla (p + \psi_g), \tag{2.3}$$

$$\mathbf{u}_w = -\lambda_w \nabla (p + \psi_w). \tag{2.4}$$

These expressions state that the flux of each fluid is proportional to the gradient of a flow potential. For single-phase flow, the potential is the same for both components— the fluid pressure. For multiphase systems the flow potentials are different because of capillary pressure effects. We split the fluid flow potentials into a global pressure p and

a capillary potential ψ_α. An analogous split was originally proposed by Otto & E (1997) and E & Palffy-Muhoray (1997) in the context of phase separation of incompressible polymer mixtures.

Adopting the classical generalization of Darcy's law to multiphase systems, we set the gas and water mobilities as

$$\lambda_g = \frac{b^2}{12\mu_g} k_{rg}(S_g), \tag{2.5}$$

$$\lambda_w = \frac{b^2}{12\mu_w} k_{rw}(S_w), \tag{2.6}$$

where μ_α is the viscosity of fluid phase α, and $k_{r\alpha}$ is the phase relative permeability. For a Hele-Shaw cell or smooth fracture, Fourar & Lenormand (1998) derived the relative permeabilities that correspond to viscous coupling between the two fluids, assuming Stokes flow in the gap and a three-layer configuration with the wetting fluid coating the walls and the non-wetting fluid inside the cell. The relative permeabilities are given by

$$k_{rw} = \frac{1}{2} S_w^2 \left(3 - S_w\right),$$
$$k_{rg} = S_g^3 + \frac{3}{2M} S_g \left(1 - S_g\right) \left(1 + S_g\right), \tag{2.7}$$

with the viscosity ratio

$$M = \frac{\mu_w}{\mu_g}. \tag{2.8}$$

Given the relative permeabilities, k_{rg} and k_{rw}, we define the gas fractional flow function, f_g, as

$$f_g = \frac{\lambda_g}{\lambda_g + \lambda_w} = \frac{k_{rg}}{k_{rg} + \frac{1}{M} k_{rw}}. \tag{2.9}$$

The fractional flow plays an important role in the structure of the displacement patterns, as it is a non-convex function of saturation (Fig. 1). After algebraic manipulation, assuming constant gap width b, density-matched fluids with constant densities, and using the gas saturation as primary variable, the model equations read

$$\partial_t S_g + \nabla \cdot \left(f_g \mathbf{u}_T + \frac{b^2}{12} \frac{k_{rw}}{\mu_w} f_g \nabla \left(\psi_w - \psi_g\right) \right) = 0, \tag{2.10}$$

$$\mathbf{u}_T = -\frac{b^2}{12} \left[\left(\frac{k_{rg}}{\mu_g} + \frac{k_{rw}}{\mu_w} \right) \nabla \pi + \frac{k_{rw}}{\mu_w} \nabla \left(\psi_w - \psi_g\right) \right], \tag{2.11}$$

$$\nabla \cdot \mathbf{u}_T = 0, \tag{2.12}$$

subject to the constraint $S_g + S_w = 1$. In the above model equations, the pressure equation is written in terms of the *total pressure*, $\pi = p + \psi_g$. We emphasize that the equations above describe the evolution of two–dimensional—gap-averaged—fields; that is vector fields are two-dimensional and saturations, pressures and velocities should be understood as gap-averaged quantities.

In this model, fluid saturations, S_α, are interpreted as the phase fields or order parameters in our formulation. A gas saturation of 1 means that the cell gap is fully occupied by gas, whereas a saturation of 0 means that it is fully occupied by water. In the following section, we discuss the modeling framework for the capillary potentials ψ_α. The above equations (2.10)–(2.12) provide the basis of a diffuse–interface or phase–field model for Hele–Shaw flow. An important element of the model that needs to be specified is a free energy functional from which the capillary potentials are derived. We discuss this topic in the following section.

2.2. *Design of the free energy functional and capillary potentials*

The capillary potentials, ψ_g and ψ_w, are defined as the variational derivatives of a heuristic free energy functional with respect to the fluid saturations (Cahn & Hilliard 1958; De Gennes 1980),

$$\psi_\alpha \equiv \frac{\delta F}{\delta S_\alpha} = \frac{\partial F}{\partial S_\alpha} - \nabla \cdot \left(\frac{\partial F}{\partial (\nabla S_\alpha)} \right). \tag{2.13}$$

The free energy F plays a central role in the dynamic and equilibrium properties of the model. To design the free energy functional, we will focus on capturing fluid segregation at steady state. We propose a free energy functional of the form

$$\begin{aligned}
F = &-\frac{\gamma_{sw} - \gamma_{sg} - \gamma}{b} \omega(S_g, S_w) + \frac{\gamma_{sw} - \gamma_{sg}}{b} \ell(S_g, S_w) \\
&+ \frac{\Gamma}{4} \kappa(S_g, S_w) \left(|\nabla S_g|^2 + |\nabla S_w|^2 \right),
\end{aligned} \tag{2.14}$$

where the functions ω and ℓ are, respectively, a double-well function, and a symmetry-breaking function describing the difference in surface energies between fluids and the solid. The surface tensions between the fluids and the solid are γ_{sw} and γ_{sg}, while the surface tension between fluids is denoted by γ. The coefficient Γ (units of force), controls the strength of the gradient-energy terms. The terms in (2.14) that do not depend explicitly on saturation gradients are collectively referred to as the bulk free energy, F_0,

$$F_0 = -\frac{\gamma_{sw} - \gamma_{sg} - \gamma}{b} \omega(S_g, S_w) + \frac{\gamma_{sw} - \gamma_{sg}}{b} \ell(S_g, S_w). \tag{2.15}$$

In the following, we consider strictly non-spreading systems, $\gamma_{sw} - \gamma_{sg} - \gamma < 0$, for which the three surface energies are linked through the static contact angle, $\gamma_{sw} - \gamma_{sg} = \gamma \cos\theta$. The structure of the function multiplying the square concentration gradients, $\kappa(S_g, S_w)$, is essential to obtain *compactons* (Benzi *et al.* 2011; Cueto-Felgueroso & Juanes 2012). Traditional phase-field models use a constant value of κ, which implies a smooth transition between 0 and 1 in the order parameter; that is, equilibrium saturation profiles approach the values 0 and 1 asymptotically on each side of the interface. If κ vanishes at $S_g = 0$ and/or $S_g = 1$, saturation profiles may have compact support, reaching 0 and/or 1 within a finite width.

Incorporating the above definitions, the full expression for the free energy reads:

$$F = \frac{\gamma(1 - \cos\theta)}{b} \omega(S_g, S_w) + \frac{\gamma \cos\theta}{b} \ell(S_g, S_w) + \frac{\Gamma}{4} \kappa(S_g, S_w) \left(|\nabla S_g|^2 + |\nabla S_w|^2 \right), \tag{2.16}$$

and the capillary potentials based on this free energy are

$$\psi_g = \frac{\gamma(1 - \cos\theta)}{b} \frac{\partial \omega}{\partial S_g} + \frac{\gamma \cos\theta}{b} \frac{\partial \ell}{\partial S_g} - \frac{\Gamma}{2} \sqrt{\kappa} \nabla \cdot \left(\sqrt{\kappa} \nabla S_g \right), \tag{2.17}$$

$$\psi_w = \frac{\gamma(1 - \cos\theta)}{b} \frac{\partial \omega}{\partial S_w} + \frac{\gamma \cos\theta}{b} \frac{\partial \ell}{\partial S_w} - \frac{\Gamma}{2} \sqrt{\kappa} \nabla \cdot \left(\sqrt{\kappa} \nabla S_w \right). \tag{2.18}$$

The rationale behind the above expressions is to satisfy the following design objectives: at steady state, the system must relax towards a segregated state, with saturations 1 and 0 separated by a transition region that does not grow in time, and whose length scale is consistent with the cell gap and wetting properties of the system (static contact angle, θ). This requirement translates into the functional form of the bulk free energy, through the common tangent construction: we require a common tangent at $S = 0$ and

$S = 1$, for all static contact angles. We adopt the following simple functional forms

$$\omega = C_\omega (1 - S_g)^\beta (1 - S_w)^2, \tag{2.19}$$

$$\ell = 2 \left[(1 - S_g)^2 - (1 - S_w)^2 \right], \tag{2.20}$$

where C_ω is a normalization constant. It is easy to show that these expressions satisfy the modeling requirements of having a common tangent at saturations $S_g{=}0$ and $S_g{=}1$ (Fig. 2 **a,b**). The exponent β in the double-well plays the role of changing the location of the inflection points in the double well, which determine the stability properties of wetting films, that is, the range of constant saturations that are stable under small perturbations. Different exponents β also introduce asymmetry in the basins associated with saturations 1 and 0, which changes the relative importance of the gradient energy terms (equation (2.21)); for large β, the relative strength of the gradient terms increases near $S_g{=}1$, where the bulk free energy becomes flatter, implying that saturations will approach $S_g{=}1$ more slowly than they do for smaller β. Conversely, saturation profiles approach $S_g{=}0$ more abruptly for larger β, because the bulk free energy becomes steeper (Fig. 2 **c,d**).

With the above expressions, the free energy functional reads

$$
\begin{aligned}
F =& C_\omega \frac{\gamma (1 - \cos\theta)}{b} (1 - S_g)^\beta (1 - S_w)^2 + 2 \frac{\gamma \cos\theta}{b} \left[(1 - S_g)^2 - (1 - S_w)^2 \right] \\
&+ \frac{\Gamma}{4} \kappa (S_g, S_w) \left(|\nabla S_g|^2 + |\nabla S_w|^2 \right).
\end{aligned}
\tag{2.21}
$$

Based on the above free energy, the common-tangent construction (Witelski 1998) yields, for arbitrary contact angles $0° {<} \theta {\leqslant} 180°$, and along $S_w{=}1{-}S_g$, the stable states $S_g{=}0$, and $S_g{=}1$ (Fig. 2). The capillary potentials are given by

$$\psi_g = -C_\omega \beta \frac{\gamma (1 - \cos\theta)}{b} (1 - S_g)^{\beta-1} (1 - S_w)^2 - 4 \frac{\gamma \cos\theta}{b} (1 - S_g) - \frac{\Gamma}{2} \sqrt{\kappa} \nabla \cdot \left(\sqrt{\kappa} \nabla S_g \right), \tag{2.22}$$

and

$$\psi_w = -2 C_\omega \frac{\gamma (1 - \cos\theta)}{b} (1 - S_g)^\beta (1 - S_w) + 4 \frac{\gamma \cos\theta}{b} (1 - S_w) - \frac{\Gamma}{2} \sqrt{\kappa} \nabla \cdot \left(\sqrt{\kappa} \nabla S_w \right). \tag{2.23}$$

The difference in capillary potentials, $\psi_w{-}\psi_g$, whose relaxation drives the saturation profiles in the static limit of equation (2.10), is given by

$$\psi_w - \psi_g = -\frac{4\gamma \cos\theta}{b} - \frac{2 C_\omega \gamma (1 - \cos\theta)}{b} S_g (1 - S_g)^{\beta-1} (1 - \frac{\beta + 2}{2} S_g) + \Gamma \sqrt{\kappa} \nabla \cdot \left(\sqrt{\kappa} \nabla S_g \right), \tag{2.24}$$

where we have used the identity $S_w{=}1{-}S_g$.

In the present model we do not consider the effect of dynamic contact angles or a dynamic capillary pressures (Park & Homsy 1984; Hassanizadeh & Gray 1993). Dynamic capillary pressure corrections have been derived from asymptotic analyses of the two-phase Hele-Shaw problem to account for wetting films (Park & Homsy 1984), and as rationalizations of the observed rate-dependency of the constitutive relations in multiphase flow through porous media (Hassanizadeh & Gray 1993). In the present formulation, these effects could be included in the form of a term in the free energy functional that depends on the rate of change of fluid saturations. This term has been suggested as a thermodynamically consistent extension of the Cahn-Hilliard model (Gurtin 1994), and in the capillary pressure function in models of multiphase porous media flow (Hassanizadeh & Gray 1993; Duijn *et al.* 2007).

2.3. *Dimensional analysis and summary of the model equations*

We identify the following dimensionless groups: a capillary number, Ca, which compares viscous and capillary forces,

$$\text{Ca} = \frac{U\mu_w}{\gamma}, \tag{2.25}$$

an anisotropy ratio, ϵ, which is the ratio of the gap thickness to the reference length, L,

$$\epsilon = \frac{b}{L}, \tag{2.26}$$

the viscosity ratio, M,

$$M = \frac{\eta_w}{\eta_g}, \tag{2.27}$$

and a Cahn number, C_Γ, controlling the strength of the gradient energy term,

$$C_\Gamma = \frac{b\Gamma}{\gamma L^2}. \tag{2.28}$$

At equilibrium we impose the balance between second and fourth-order terms in the static limit of (2.10),

$$\Gamma \sim \frac{\gamma L^2}{b}, \tag{2.29}$$

so that the characteristic interface thickness is approximately the gap width $\delta \sim b/L$. In dimensionless quantities, the equation for the non-wetting phase saturation reads

$$\partial_t S_g + \nabla \cdot \left(f_g \mathbf{u}_T + \frac{\epsilon}{12\text{Ca}} k_{rw} f_g \nabla \left(F_0' + C_\Gamma \sqrt{\kappa} \nabla \cdot \left(\sqrt{\kappa} \nabla S_g \right) \right) \right) = 0, \tag{2.30}$$

where the dimensionless total Darcy velocity of the mixture is

$$\mathbf{u}_T = -\frac{\epsilon}{M\text{Ca}} \left[\left(k_{rg} + \frac{1}{M} k_{rw} \right) \nabla \pi + \frac{1}{M} k_{rw} \nabla \left(F_0' + C_\Gamma \sqrt{\kappa} \nabla \cdot \left(\sqrt{\kappa} \nabla S_g \right) \right) \right], \tag{2.31}$$

where $\pi = p + \psi_g$ and we require $\nabla \cdot \mathbf{u}_T = 0$, which yields an elliptic equation that must be solved to obtain the pressure field, p. In the above equations, F_0' denotes the dimensionless derivative of the bulk free energy,

$$F_0' = -4\cos\theta - 2C_\omega \left(1 - \cos\theta \right) S_g (1 - S_g)^{\beta-1} (1 - \frac{\beta+2}{2} S_g). \tag{2.32}$$

Assuming $\kappa = 1$, $\theta = 180°$, $\beta = 8$, $C_\omega = 4$, and adopting as reference length the gap width $L \equiv b$, so that the anisotropy ratio and characteristic transition width are equal to one, $\epsilon = \delta = 1$, the saturation equation and total velocity reduce to

$$\partial_t S_g + \nabla \cdot \left(f_g \mathbf{u}_T + \frac{1}{12\text{Ca}} k_{rw} f_g \nabla \left(-16 S_g (1 - S_g)^7 (1 - 5 S_g) + C_\Gamma \nabla^2 S_g \right) \right) = 0, \tag{2.33}$$

and

$$\mathbf{u}_T = -\frac{1}{M\text{Ca}} \left[\left(k_{rg} + \frac{1}{M} k_{rw} \right) \nabla \pi + \frac{1}{M} k_{rw} \nabla \left(-16 S_g (1 - S_g)^7 (1 - 5 S_g) + C_\Gamma \nabla^2 S_g \right) \right], \tag{2.34}$$

respectively. Note that we dropped the constant term in F_0', and that the pressures p and ψ_g were made dimensionless, with characteristic pressure $p_c = \gamma/b$. In the pressure equation, we solve for the total pressure, π rather than for p. Once π is solved for, the pressure p can be recovered using equation (2.22) for the gas capillary potential, which is a function of saturation and its derivatives.

In the model equations above, and throughout the analysis and sample simulations presented in this paper, we set the function κ to be a constant, $\kappa=1$, for computational convenience. While not changing the results qualitatively, this choice implies that, strictly, solutions do not have compact support at equilibrium or during dynamic displacements; saturation profiles approach $S_g=0$ and $S_g=1$ smoothly. Another consequence for dynamic displacements is the need for a small, artificial "precursor film" of the invading fluid, in analogy to the precursor film needed in driven thin films under the standard formulation.

3. Simulation results

3.1. *One-dimensional displacements.*

To illustrate the structure of the displacement patterns, we start by considering, in a 1D setting, a constant-rate injection case. In this flow scenario, the total velocity is uniform and constant in time. In dimensionless quantities, gas saturations evolve according to the nonlinear, fourth-order scalar conservation law

$$\partial_t S + \partial_x f_g + \partial_x \left(\frac{1}{12\mathrm{Ca}} k_{rw} f_g \partial_x \left(F_0' + C_\Gamma \partial_{xx} S \right) \right) = 0, \tag{3.1}$$

where $S \equiv S_g$ is the gas saturation. In the equation above we take the gap width as reference length, $L=b$, and therefore the anisotropy ratio equals one, $\epsilon=1$. With the relative permeabilities of equations (2.7), the gas fractional flow is

$$f_g = \frac{k_{rg}}{k_{rg} + \frac{1}{M} k_{rw}} = \frac{S^3 + \frac{3}{2M} S \left(1 - S \right) \left(1 + S \right)}{S^3 + \frac{3}{2M} S \left(1 - S \right) \left(1 + S \right) + \frac{1}{2M} \left(1 - S \right)^2 \left(2 + S \right)}. \tag{3.2}$$

We further set $\beta=8$ in the double-well function (2.19) and $\cos\theta=-1$, so that the derivative of the dimensionless bulk free energy is simply

$$F_0' = -16S(1 - S)^7(1 - 5S). \tag{3.3}$$

Finally, we set $\kappa=1$ and $C_\Gamma=1/80$, which yield interface widths in the order of the gap width, $\delta\approx1$. We solve the above equation using finite differences and a fully implicit time-stepping. Explicit time-stepping is essentially precluded in PDEs with with term of order larger than second, because of the extremely restrictive stability condition; for a fourth-order equation like (3.1) the time step for an explicit method scales like Δx^4, where Δx is the grid size.

A salient feature of the solutions to our model of flow in a Hele-Shaw cell is the presence of non-classical shocks, and that the structure of the solution and displacement pattern depends strongly on the capillary number (Fig. 3). Mathematically, this feature is due to the presence of the fourth-order spatial term in equation (3.1), which combined with the free energy inducing phase segregation at equilibrium leads to undercompressive shock solutions —a plateau whose height depends on the capillary number (Fig. 3). Non-classical shocks also arise in thin film flows with Marangoni effects (Bertozzi *et al.* 1998, 1999; Bertozzi & Shearer 2000), and in theories of multiphase flow in porous media with dynamic capillary pressure (Duijn *et al.* 2007; Fan & Pop 2011).

The physical interpretation of rate-dependent incomplete displacements in the gap is well-established. When a viscous fluid is displaced by another one at constant injection rate in a capillary tube or narrow channel, the displacement pattern and efficiency depend strongly on the capillary number and viscosity ratio Bretherton (1961). In our simulations, the domain is initially saturated with the wetting fluid (water, $S=0$), and we inject the non-wetting fluid (gas, $S=1$) from the left boundary. The solution comprises

an undercompressive shock and a rarefaction wave (Fig. 3 **a,c,e**). For this flow set-up, the classical Lax shock (Lax 1957) —the solution in the hyperbolic limit— is given by a shock with speed obtained from the tangent construction. In our model shocks are undercompressive, and given by secant lines whose slope decreases with decreasing capillary numbers (Fig. 3 **b,d,f**). The discontinuity in wave speed leads to a constant saturation state, that is a plateau in the saturation profile. The presence of the plateau indicates an incomplete fluid displacement, and determines the amount of viscous fluid that is left behind in a well-developed flow under constant flow rate.The height of the plateau increases with decreasing capillary number, in accordance with experimental evidence. For a given capillary number, the height of the plateau increases with decreasing viscosity contrast, since the Lax shock would already yield a larger shock amplitude. This behavior is due to the structure of the fractional flow; the slope of the tangent from the origin decreases with decreasing viscosity contrast.

3.2. *Traveling wave analysis. Traveling bubbles*

An important practical and theoretical issue is whether our model can predict traveling bubbles and, if so, under what conditions these bubbles are stable. Experimental observations show that a bubble that is transported under constant flow rate of the ambient fluid flow in a Hele-Shaw cell will reach an equilibrium shape and travel downstream at constant speed (Kopf-Sill & Homsy 1988a). Mathematically, traveling bubbles imply the existence of traveling wave solutions with undercompressive shocks (Bertozzi *et al.* 1999; Bertozzi & Shearer 2000; Strait *et al.* 2013). In the context of multiphase flow in porous media, undercompressive traveling waves have been recently analyzed by Strait *et al.* (2013) for two-phase flow in capillaries, showing the existence of compactly-supported traveling waves when κ vanishes at $S_g = 0$. Here we investigate numerically whether our model can predict this behavior, and perform a study of the traveling wave solutions to the 1D model equation (3.1) to rationalize the behavior observed when solving the full PDE.

To illustrate the difficulty of achieving traveling bubbles within a fractional flow formulation, we illustrate the set-up in the context of the hyperbolic limit of equation (3.1) (Ca$\rightarrow\infty$). In that case, the model reduces to

$$\partial_t S + \partial_x f_g = 0. \tag{3.4}$$

For simplicity, we study the displacement of a square gas saturation profile, representing a bubble, by the constant-rate injection of a viscous fluid (Fig. 4). At early times, the solution comprises two shocks and rarefaction waves. Since the rear shock is faster than the leading-front shock, the solution at late times is a shock at the leading edge, and a rarefaction wave. Clearly, this type of solutions does not describe a traveling bubble.

In contrast to the classical hyperbolic model, our model yields two types of solution profiles depending on the capillary number (Fig. 5). For small capillary numbers (Fig. 5 **a,c**), the slope of the secant to the fractional flow is smaller than the slope of the fractional flow at the origin. A traveling bubble thus arises from front and rear shocks that have the same speed. At high capillary numbers (Fig. 5 **b,d**), the slope of the secant line is significantly larger than the slope of the fractional flow at the origin. The rear shock does not return back to the origin, and another plateau appears also at the back of the bubble. This behavior may be consistent with shedding bubbles at the trailing edge observed in experiments (Kopf-Sill & Homsy 1988a). The shape of displaced bubbles varies with capillary number, as in the case of constant-rate gas injection, consistently with the overall trend of smaller plateau heights and less efficient displacements for larger capillary numbers (Fig. 6).

The particular conditions leading to the existence of traveling bubbles, as well as their structure, can be rationalized by computing the traveling wave solutions to our model equation (3.1). Traveling wave analysis also helps understand the structure of the undercompressive shocks obtained in the previous section by solving the PDE problem. We therefore seek solutions to (3.1) in a moving reference frame, defining the coordinate $\xi = x - Vt$, where V is the characteristic wave speed. Expressing space and time derivatives as derivatives with respect to ξ,

$$\partial_x(\cdot) = \partial_\xi(\cdot), \quad \partial_t(\cdot) = -V\partial_\xi(\cdot), \tag{3.5}$$

and integrating once, equation (3.1) becomes a third-order ordinary differential equation for $s(\xi) \equiv S(x - Vt)$,

$$V(s^L - s) + (f_g - f_g^L) + \frac{k_{rw}f_g F_0''}{12\mathrm{Ca}}s_\xi + \frac{C_\Gamma}{12\mathrm{Ca}}k_{rw}f_g s_{\xi\xi\xi} = 0, \tag{3.6}$$

where the left state is defined as $s^L = s(\xi \to -\infty)$, we assumed vanishing derivatives as $\xi \to -\infty$, and the characteristic speed V is given by the jump condition

$$V = \frac{f^L - f^R}{s^L - s^R}. \tag{3.7}$$

For convenience, we write the above third-order ODE as a system of first-order ODEs in the variables $(s, u, v) \equiv (s, s_\xi, s_{\xi\xi})$, as

$$\begin{aligned}
s_\xi &= u, \\
u_\xi &= v, \\
v_\xi &= -\frac{12\mathrm{Ca}}{C_\Gamma}\frac{f_g - f_g^L - V(s - s^L)}{k_{rw}f_g} - \frac{F_0''}{C_\Gamma}u
\end{aligned} \tag{3.8}$$

We compute the traveling waves by integrating forward in ξ using a standard explicit Runge-Kutta solver, with the initial condition $(s^L, 0, 0)$ plus a small perturbation to start the orbits. Note that obtaining traveling waves requires iterating to find the correct pairs (s^L, Ca) or (Ca, V). That is, for each capillary number there is a corresponding left state, or plateau height, s^L, for the Riemann problem, or a characteristic speed in the case of homoclinic orbits. For constant κ, we need to assume a non-zero precursor, because $(s, u, v) = (0, 0, 0)$ is not a stable equilibrium of the above dynamical system. To understand the behavior near $s = 0$, we note that $f_g(s \to 0) \sim \frac{3}{2}s$ and $k_{rw}(s \to 0) \sim 1$. This implies that, if we take $s^R = 0$ and near $s = 0$, the dynamical system behaves like

$$\begin{aligned}
s_\xi &= u, \\
u_\xi &= v, \\
v_\xi &= -\frac{12\mathrm{Ca}}{C_\Gamma}\left(\frac{3}{2} - V\right) - \frac{F_0''}{C_\Gamma}u.
\end{aligned} \tag{3.9}$$

Analogously to driven thin film problems, this precursor films becomes a numerical parameter. We set this precursor to be $s^R = 10^{-4}$ in the calculation of the characteristic speeds (3.7).

We identify three families of traveling wave solutions, depending on the left state, s^L, and on whether we seek for heteroclinic or homoclinic orbits (Fig. 7, top row). Type I traveling waves correspond to the solution of the Riemann problem with varying left state and fixed, small right state, $s^R = 10^{-4}$ in the present case. These traveling waves can be compared with the plateau of the constant-flux displacements computed by solving the PDE (Fig. 3). Type II waves are homoclinic orbits, connecting $s^L = s^R$. Type III waves,

which may be interpreted as rear fronts in the water-gas displacements, connect a small left state, s^L, with an asymptotic right state s^R.

Using these three families of traveling waves, we may elucidate the structure of constant-volume gas displacements, and the conditions leading to the existence of traveling bubbles, that is, local structures that travel at constant speed preserving their shape. When a finite volume of gas is displaced by water (as in Figs. 5–6), two fronts will form at the front and rear of the bubble. If the speed of the front shock is larger than that of the rear shock, conservation of mass implies that traveling bubbles may not exist, and a trailing fluid film is left behind. The crossover corresponds to the critical capillary number, Ca_c, beyond which Type I waves are faster that Type II and Type III waves (Fig. 7, bottom). The critical capillary number depends on the viscosity contrast, M, and on the shape of the relative permeabilities and bulk free energy (through the parameter β). For $M{=}200$ and $\beta{=}8$, the crossover criterion predicts $Ca_c{\approx}0.01$, which is similar to the capillary number beyond which a secondary plateau is found when solving the PDE (Fig. 6).

This rear plateau may be interpreted as a trailing "film" of the bubble fluid that is left behind. In the case of a gas bubble this film would be unphysical, pointing to the limits of applicability of the present model, or may be interpreted as a breakup instability of the bubbles, which could be contrasted with experiments. To understand the height of the rear plateau as a function of the capillary number, we note that its appearance is explained by the fact that the leading front of the bubble is faster than the rear front. The plateau height may therefore be determined by the need to connect a suitable Type III rear wave with a Type I wave corresponding to the leading front. For a given capillary number, the speed of Type III traveling waves increases with increasing left states s^L (Fig. 8 **a, b**). Therefore the way to connect to a faster Type I front wave is to develop a rear plateau such that the speed of the corresponding Type III wave matches that of the front wave. The set of crossing points between the curve of Type I speeds as a function of capillary number, and curves of Type III waves for different Ca and left state s^L (Fig. 8 **a**) determines the increasing heights of the rear plateau as Ca increases, in accordance with the PDE simulation results.

The shape of the double-well function (2.19) determines the range of capillary numbers for which traveling waves can be found. While a complete analysis is beyond the scope of the present study, we note that smaller values of the exponent β lead to a reduced range of capillary numbers for which traveling waves exist. As the value of β decreases, the height of the plateau for a given Ca increases (Fig. 9). The viscosity contrast between the two fluids, M, also impacts the structure of the traveling wave solutions (Fig. 10). For a given capillary number, the speed of the traveling waves increases with M, which is consistent with the higher plateau, as observed in the PDE solutions (Fig. 3 **a,c,e**).

3.3. *Two-dimensional bubble motion*

In this section, we extend the one-dimensional results of the previous section to full two-dimensional examples of bubble motion. To compute numerical solutions of the model equations (2.10)–(2.12), we adopt a sequential solution approach where we first advance the fluid saturations, and then update the pressures and velocities by solving the elliptic problem (2.11)–(2.12). For the transport problem (2.10), we use high-order finite differences in space and the biharmonic-modified time-stepping method of Bertozzi *et al.* (2011) for fourth-order nonlinear diffusion equations. For the pressure problem, (2.11)–(2.12), we use a finite volume formulation with simple two-point flux approximations.

We simulate the motion of bubbles driven by constant-rate injection of a more viscous ambient fluid. We study the impact of capillary number and viscosity contrast, as well as the impact of confinement, by varying the cell width and bubble size. For small capillary

numbers, the bubbles adopt a nearly circular shape, which is distorted as the capillary number increases. The gas saturation inside the bubbles is also larger for smaller capillary numbers, indicating thinner films of the ambient wetting fluid adhered to the cell walls (Fig. 11). Larger viscosity ratios yield more elongated bubbles, which are thinner and thus travel at higher speeds (Figs. 12). In the absence of confinement, high capillary numbers lead to bubble breakup, splitting into two or more smaller bubbles (Fig. 13). The initial gas volume is important to understand the impact of boundary confinement and stability of the bubbles (Fig. 14). For the explored system parameters, we do not observe the flattened or "Tanveer" bubbles (Kopf-Sill & Homsy 1988*a*), but a more thorough analysis of the model is needed to fully understand the dependence of bubble shape and speed on viscosity contrast, wetting properties of the system, bubble size, and pressure-driven versus gravity-driven displacements.

3.4. *Viscous fingering*

The instability of driven fronts in two-phase flow when the invading fluid is less viscous than the defending one is a classical problem in fluid mechanics (Saffman & Taylor 1958*b*; Park & Homsy 1984, 1985; Homsy 1987; Kopf-Sill & Homsy 1988*b*; Arnéodo *et al.* 1989). The instability that ensues, often called viscous fingering, is a paradigmatic case of pattern formation in nonlinear systems. Viscous fingering impacts the displacement efficiency in multiphase flow through porous media, due to channeling and the subsequent creation of preferential flow paths. Because of these preferential paths, the sweep efficiency is significantly reduced in the presence of fingering instabilities.

We simulate viscous fingering in two-phase displacements in a Hele-Shaw cell (Figs. 15–18, see also Supplementary Movie 1). For viscosity-matched fluids the displacement front is stable, and initial perturbations of the fluid-fluid front decay exponentially (Fig. 15). At low capillary numbers, a single finger—the Saffman-Taylor finger—dominates the flow (Saffman & Taylor 1958*b*). The problem of finger width selection as a functional of system parameters is still a fascinating open problem (Moore *et al.* 2002). The classical ramified structures arise for large viscosity ratios and capillary numbers Kopf-Sill & Homsy (1988*b*); Arnéodo *et al.* (1989) (Fig. 17). Geometric confinement plays an important role in the structure of the displacement and characteristic finger size. Thus, a narrower cell imposes a constraint of the pressure dissipation, leading to finger shielding and thicker fingers. As the cell width increases, more ramified structures appear and finger widths decrease. Our model can reproduce pinch-off and reconnection events, which are typically observed in experiments of viscous fingering (Fig. 18, see Supplementary Movie 1).

4. Conclusions

We have proposed a phase-field model of two-phase flow in Hele-Shaw cells. The distinctive feature of our model is that it is a gap-averaged formulation that is designed to capture 3D effects. The model is derived within the framework of the generalized Darcy's law, with relative permeabilities that incorporate the viscous coupling (Stokes flow) in the gap. This leads to a non-convex fractional flow function that depends on the viscosity contrast. The local capillary coupling between the fluids, resulting from fluid-fluid surface tension and the wetting properties of the system, is modeled with an extension of the classical Cahn-Hilliard approach to the free energy of non-uniform systems. We design the bulk free energy to induce fluid segregation at equilibrium, and the gradient free energy leads to fourth-order spatial terms. The solutions to our model exhibit rich behavior, with displacement patterns that depend strongly on the capillary number
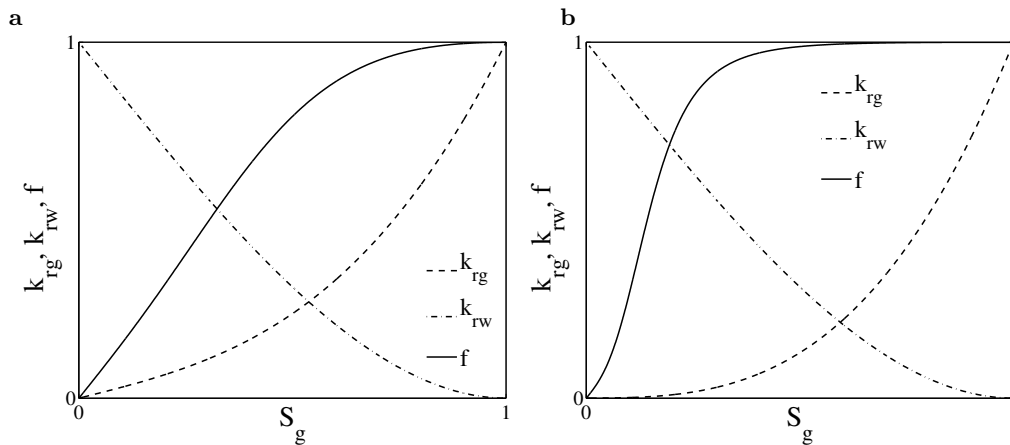
a

b

FIGURE 1. Relative permeabilities and fractional flow function for two-phase flow in a Hele-Shaw cell, assuming Stokes flow in the gap (Fourar & Lenormand 1998). These functions depend on the viscosity contrast between the fluids, $M = \mu_w/\mu_g$. **a**, $M = 5$ and **b**, $M = 200$. The shape of the fractional flow function controls the behavior of the model in the limit of large flow rates (or high capillary numbers).

and viscosity contrast, in agreement with experimental observations. As future extensions, we anticipate the application of the present modeling approach to multiphase flow through porous media (Cueto-Felgueroso & Juanes 2008) and rough fractures, which can be conceptualized as Hele-Shaw cells with variable gap width, and the consideration of buoyancy due to non-horizontal fracture orientation and density differences between the fluids. Our model naturally allows us to explore the impact of the wetting properties of the system on the displacement patterns.

5. Acknowledgements
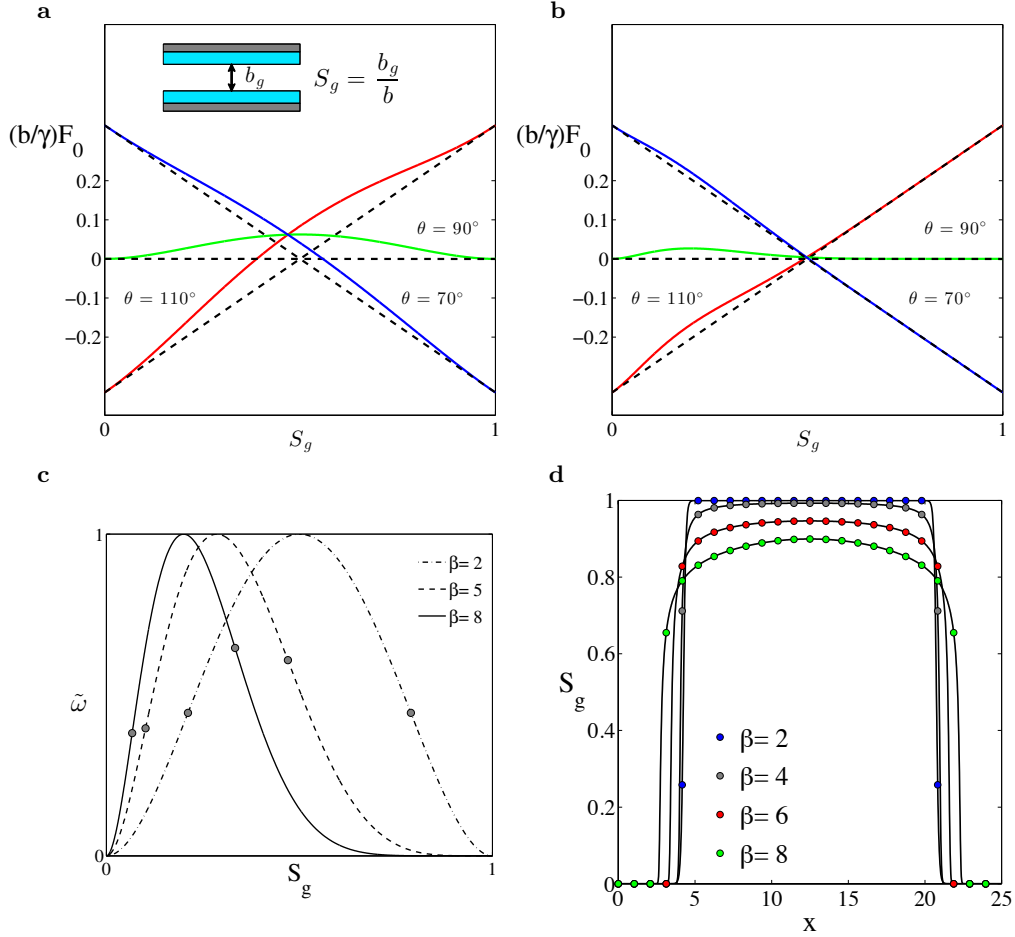
FIGURE 2. Structure of the bulk free energy in our phase-field model of two-phase flow in a Hele-Shaw cell, and its impact on the equilibrium saturation profiles. **a**, **b**, Bulk free energies for $\beta=2$ and $\beta=8$, respectively, for various static contact angles θ (from equation (2.15)). These energies satisfy that the common-tangent construction yields the correct stable states, $S_g=0$ and $S_g=1$ (dashed lines). **c**, Double-well component of the free energy, $\omega=(1-S_g)^\beta(1-S_w)^2$, normalized with respect to the maxima, $\tilde{\omega}=\omega/\max(\omega)$. As the power β increases, the spinodal region (the range of saturations between inflection points, marked with gray dots), moves towards $S_g=0$, allowing stable, relatively thick wetting films. Another consequence of different exponents is the behavior of the solution near $S_g=1$. Since the bulk free energy is flatter near $S_g=1$ and steeper near $S_g=0$ for larger β, the relative impact of the gradient energy terms in equation (2.21) becomes asymmetric, that is for large β the relative strength of the gradient energy terms is much larger near $S_g=1$, implying that saturations will approach $S_g=1$ more slowly than they approach $S_g=0$. **d**, One-dimensional, steady-state saturation profiles for gas bubbles at equilibrium, showing the impact of the exponent β on the structure of the transition from $S_g=1$ to $S_g=0$. Saturation profiles approach $S_g=0$ more abruptly for larger β, and approach $S_g=1$ more smoothly.
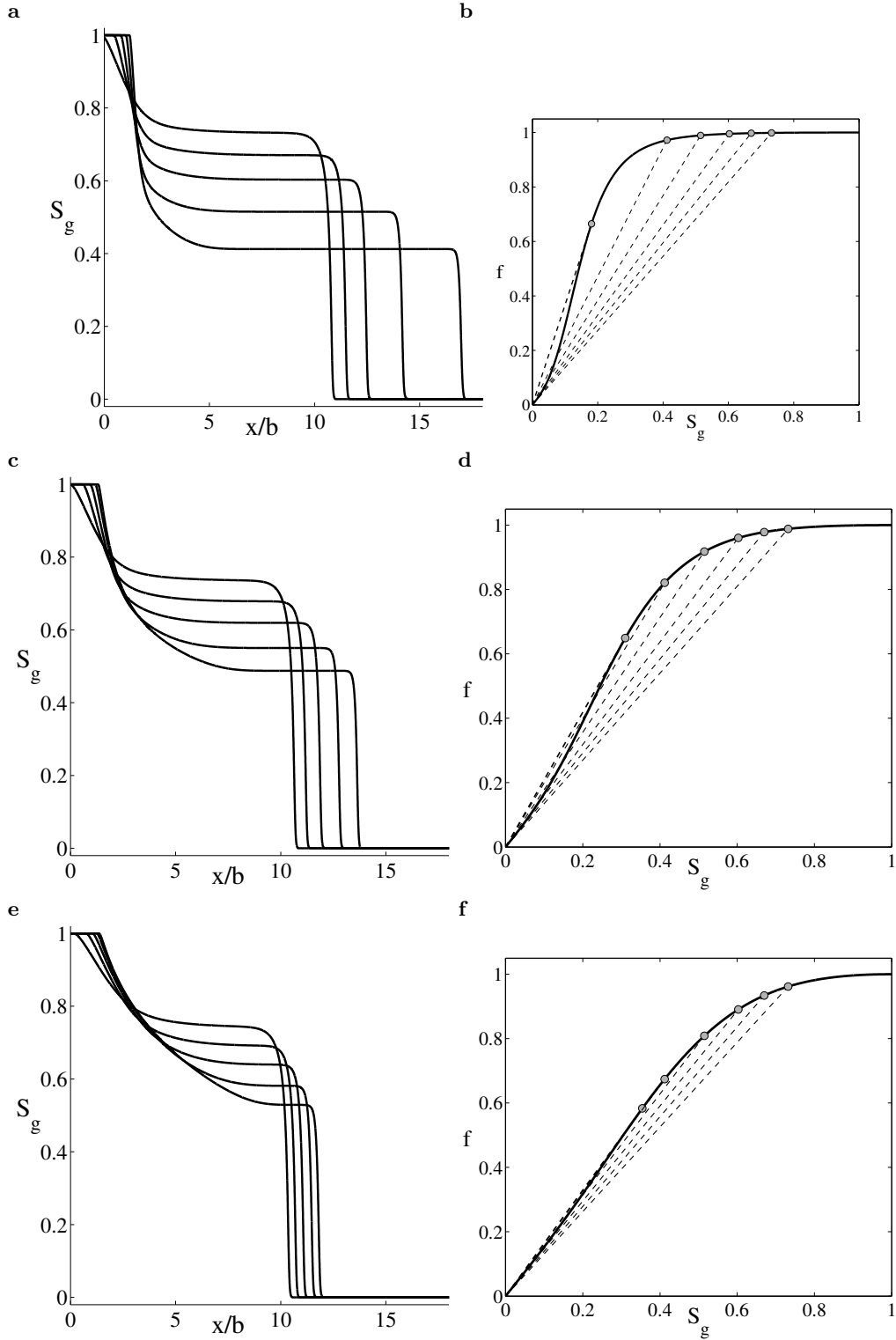
FIGURE 3. Gas saturation profiles at dimensionless time t=6.5 and capillary numbers Ca $= 1/3, 1/12, 1/60, 1/300, 1/2000$ (with increasing plateau heights). The viscosity contrast is M=200 (**a**–**b**), M=20, (**c**–**d**), and M=5 (**e**–**f**). Right column. Schematic representation of the structure of the displacement profile. For each viscosity contrast, we plot the fractional flow function and secant lines describing the undercompressive shocks. The slope of the secant lines decreases with decreasing capillary number, corresponding to increasing plateau heights.
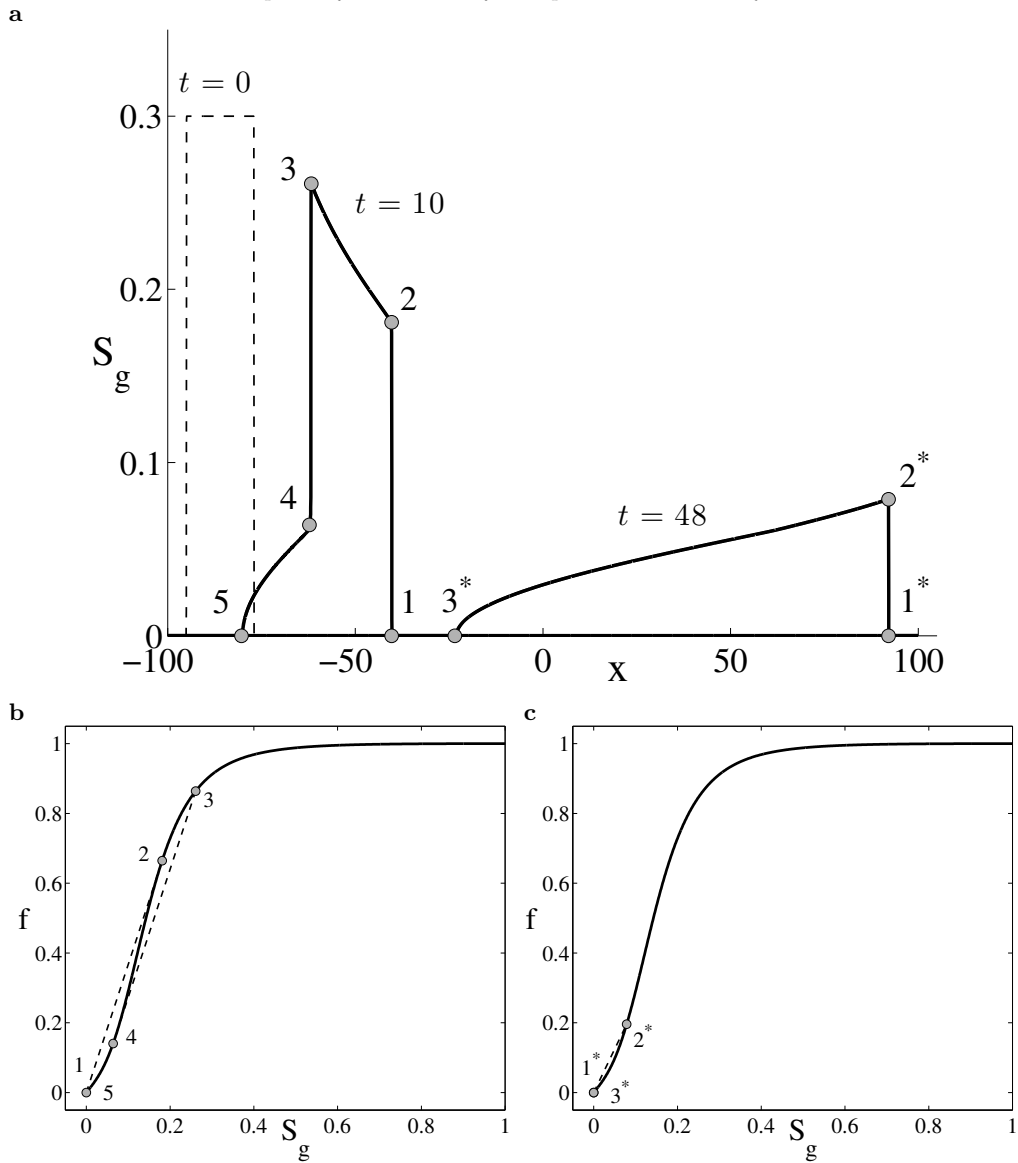
FIGURE 4. Displacement of a gas bubble in the hyperbolic limit (first-order terms only in eq. (3.1)), for M=200 and the relative permeabilities (2.7). **a**, saturation profiles at times t =0, 10 and 48. **b**, fractional flow interpretation of the saturation profile at time t=10. **c**, fractional flow interpretation of the saturation profile at time t=48.

a

b

c

d
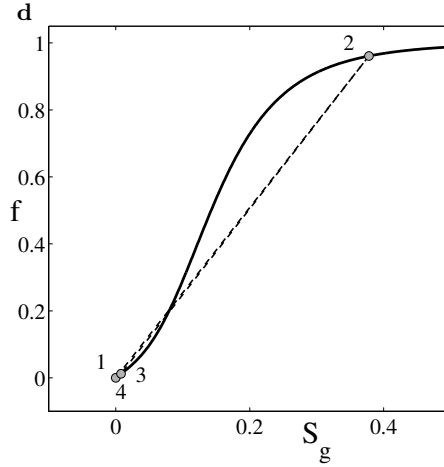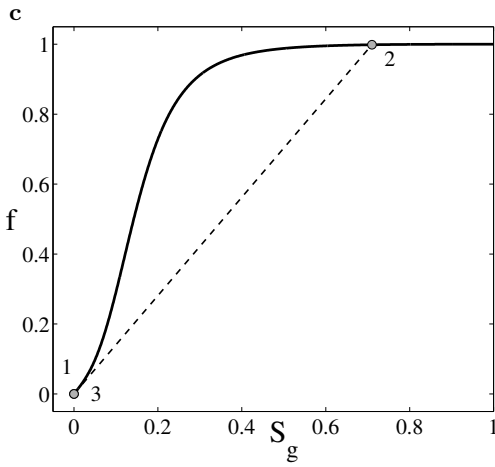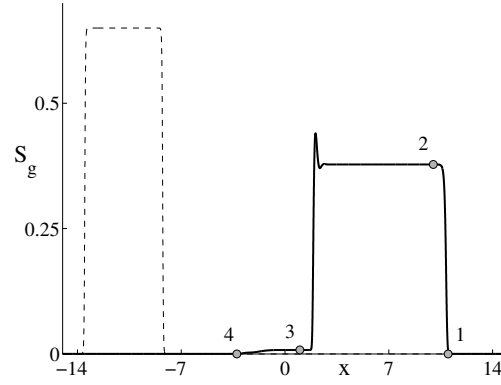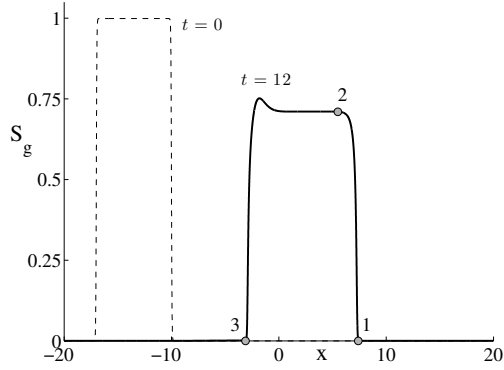
FIGURE 5. Displacement of a gas bubble for finite capillary numbers (the full model, eq. (3.1)). **a**–**c**, gas saturation profile for Ca=0.001 and M=200. **b**–**d**, gas saturation profile for Ca=0.5 and M=200. These results suggest that traveling bubbles exist for low capillary numbers.

a

b

c
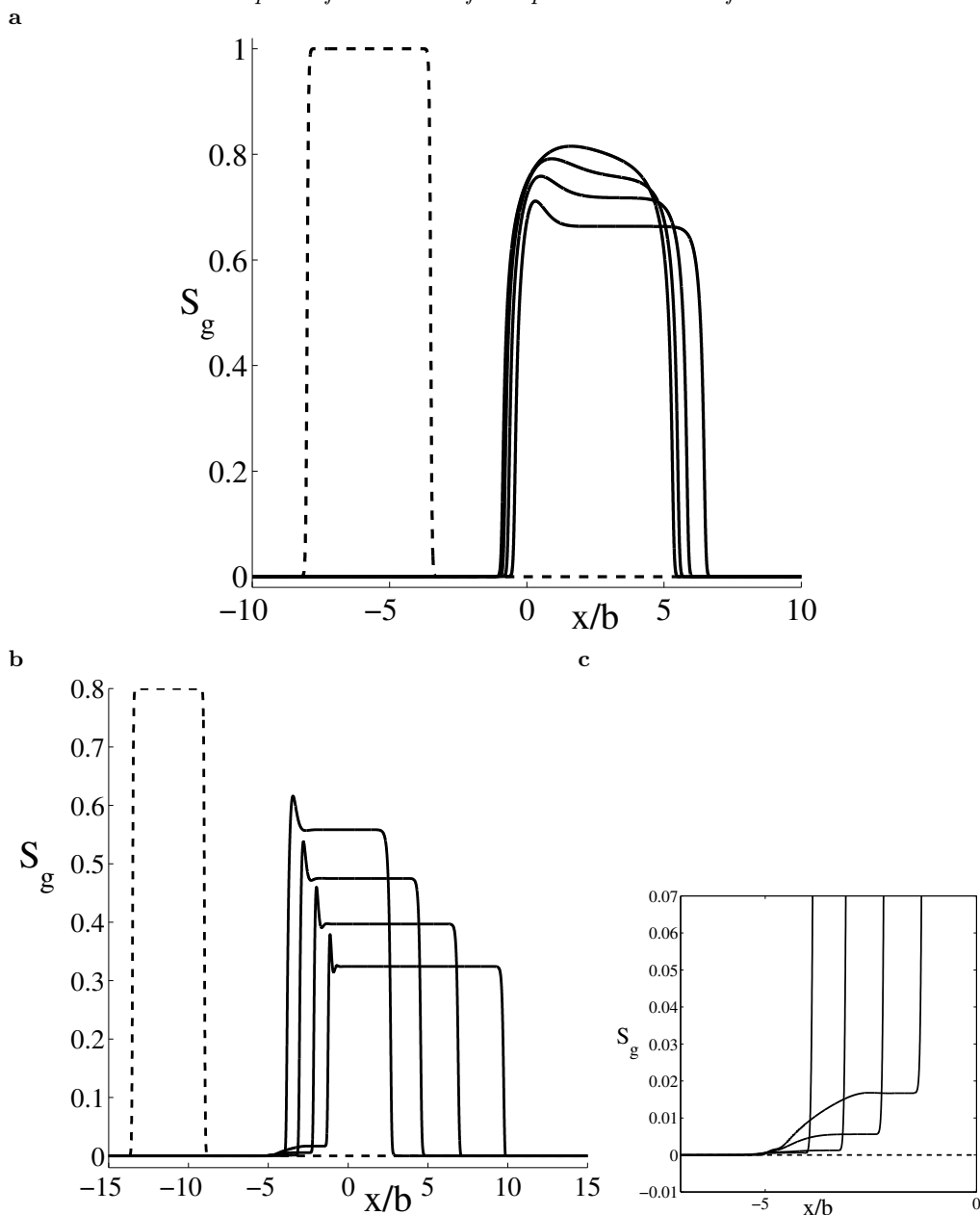
FIGURE 6. Traveling bubbles in 1D. **a**, For small capillary numbers, our model allows for traveling bubbles, that is, saturation profiles that are advected with constant speed without altering their shape. Here we show gas saturation profiles for viscosity contrast M=200 and capillary numbers Ca=4×10^{-3}, 8×10^{-4}, 2×10^{-4}, 4×10^{-5} (increasing plateau heights). **b**, At high capillary numbers, the solutions are not traveling bubbles, and the profile exhibits a complex structure. Here we show saturation profiles for capillary numbers Ca=1, 0.4, 0.15, 0.04 (increasing plateau heights). The rear front exhibits another plateau and a rarefaction wave, according to the description of Fig. 5.
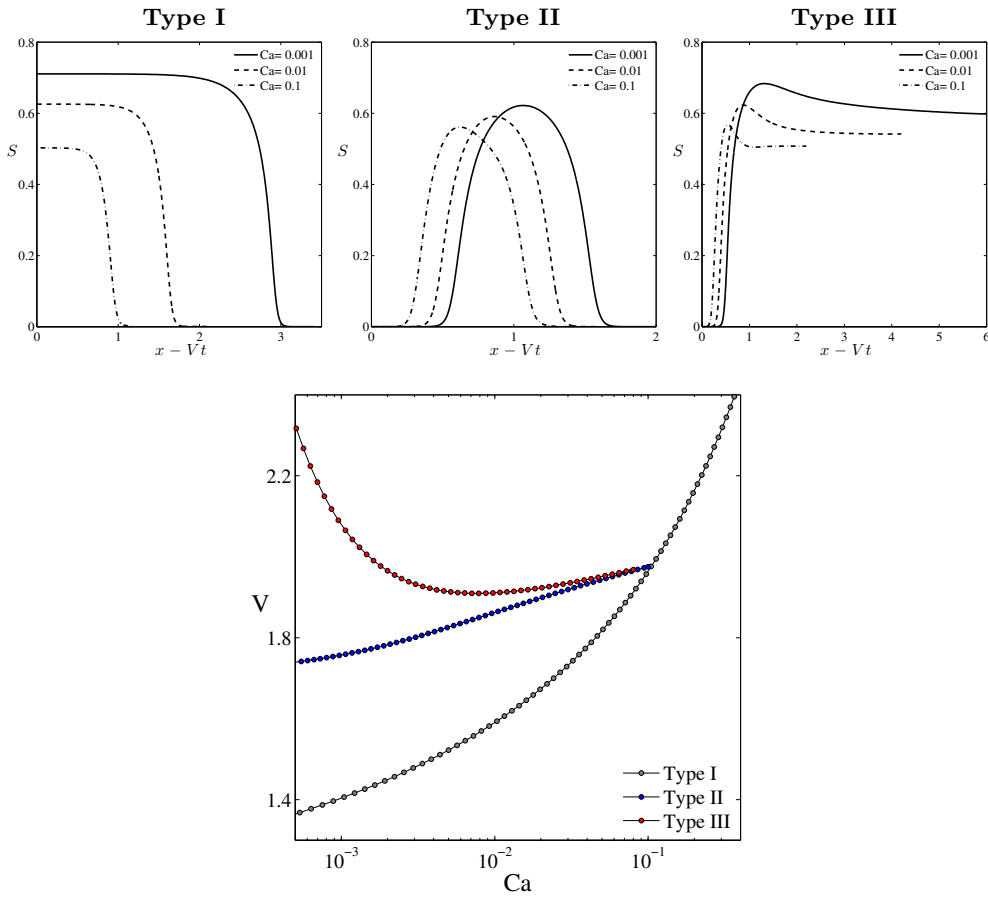
FIGURE 7. Traveling wave solutions to the one-dimensional model eq. (3.1), and their relationship with the existence of traveling bubble solutions. These results correspond to $\beta=8$ and $M=200$. Type I waves connect a left state (s^L) with a right state $(s^R=10^{-4})$. These traveling waves correspond the plateau observed in the PDE solutions of Fig. 3. Type II waves are homoclinic orbits. Type III waves connect a left state $(s^L=10^{-4})$ with a right state s^R. For a given capillary number, traveling bubbles are possible if the speed of the corresponding Type I wave is smaller that that of the Type II and II waves. Bottom, wave speed as a function of the capillary number. The critical capillary number is $Ca_c \approx 0.104$. Beyond this Ca the leading front would be faster that the rear front, and traveling bubbles do not exist: the solution will develop a secondary plateau of the bubble.
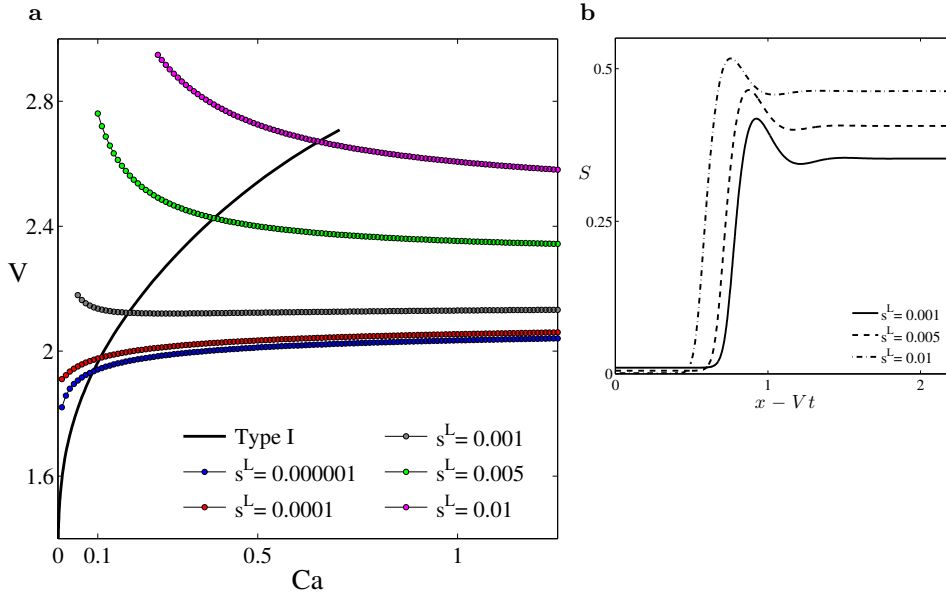
FIGURE 8. Relationship between the capillary number and the structure of the rear front for $\beta=8$ and $M=200$. Beyond a critical capillary number Ca_c, the leading front of the bubble is faster than the rear front, and the solution will develop a secondary plateau at the rear of the bubble (Figs. 6 and 7). **a,** The height of this plateau is determined by the need to connect with the Type I wave corresponding to the leading front. The speed of Type III traveling waves increases with increasing left states s^L. For a given capillary number, the height of the rear plateau is given by the Type III wave with the same speed as the Type I wave, i.e. by the crossing point of the lines in (**a**). This leads to increasing heights of the secondary plateau as Ca increases (**b**), in accordance with the PDE simulation results (Fig. 6).
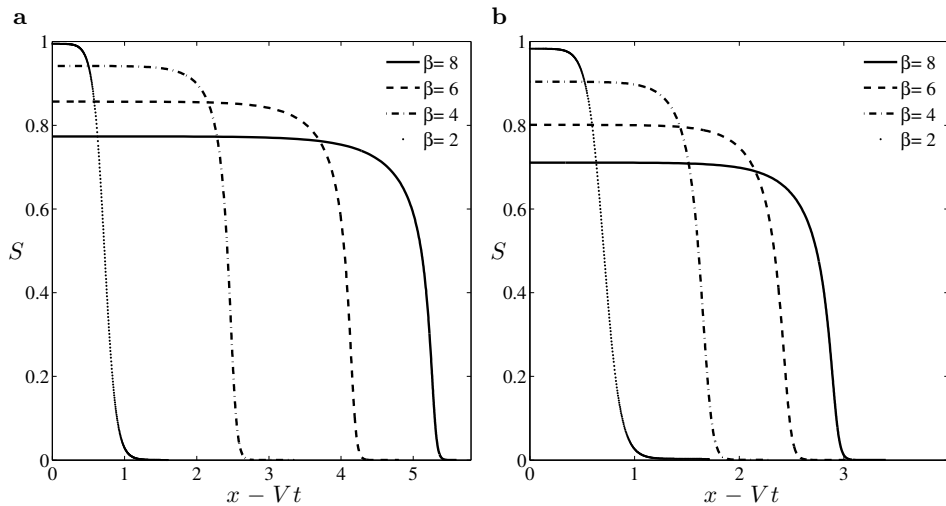
FIGURE 9. Influence of the shape of the double-well energy function on the traveling wave solutions (through the exponent β in equation (2.19)), for $M=200$. As the inflection points move towards $S_g=0$ (increasing β), the height of the plateau decreases for the same capillary number. Larger β also corresponds to a wider range of capillary numbers for which stable traveling waves exist. Sample traveling waves for **a,** Ca$=10^{-4}$, and **b,** Ca$=10^{-3}$.
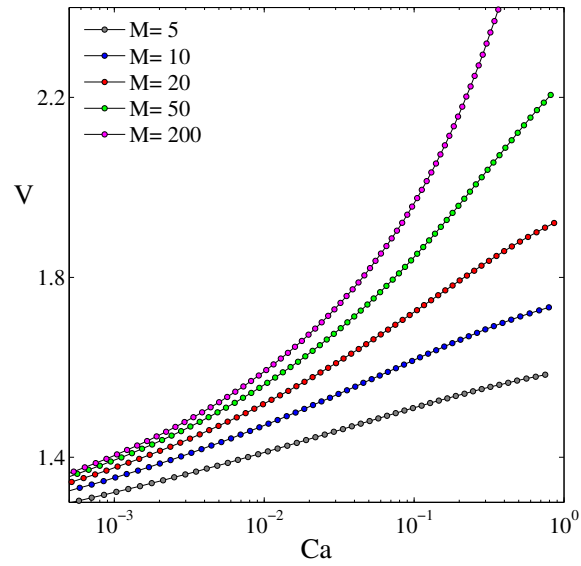
FIGURE 10. Influence of the viscosity contrast, M=μ_w/μ_g, on the speed of the Type I traveling waves, as a function of capillary number, Ca. We set $\beta = 8$. This plot elucidates the structure of the constant flux displacements obtained by solving the PDE (Fig. 3). For a given capillary number, the speed of the plateau increases with viscosity contrast. In terms of displacement pattern, this corresponds to lower plateau heights.
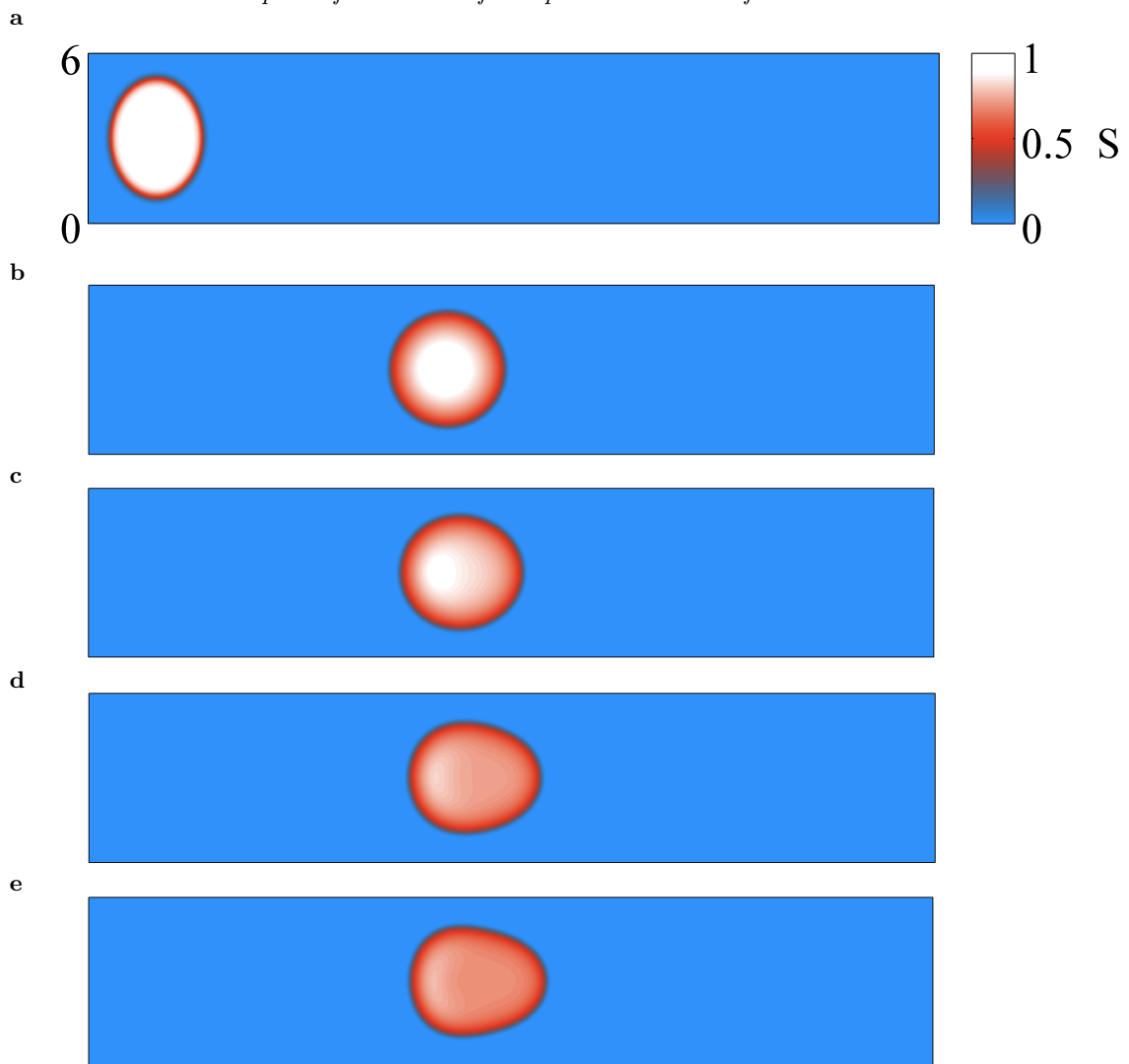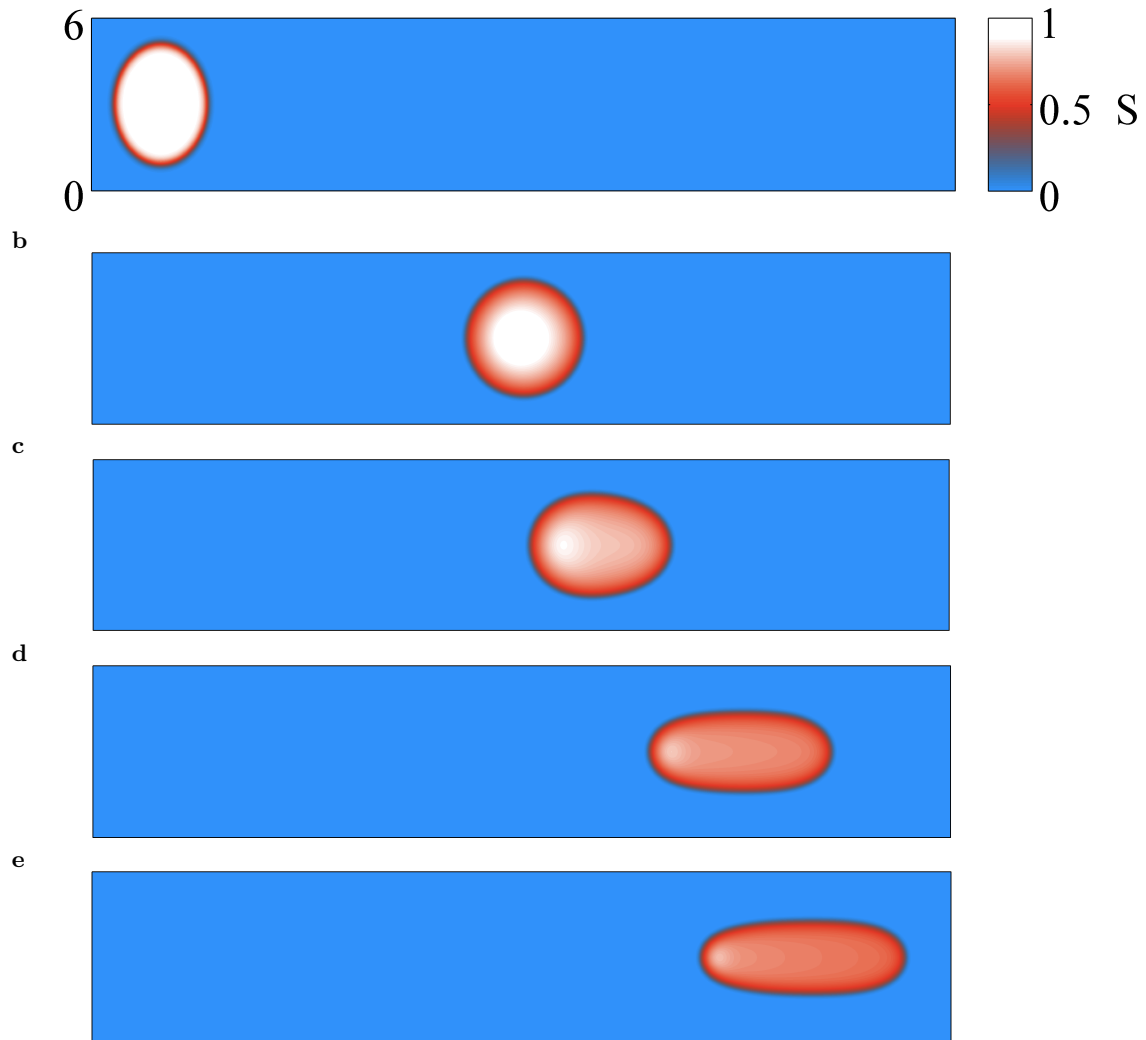
FIGURE 11. Two-dimensional simulations of a bubble flowing in a Hele-Shaw cell at low Ca. The width of the cell is $W = 6$, the viscosity contrast is $M = 5$ and the dimensionless time is $t = 7$. **a**, Initial condition; **b**, Ca = 0.0001; **c**, Ca = 0.001; **d**, Ca = 0.005; and **e**, Ca = 0.01.

FIGURE 12. Two-dimensional simulations of a bubble flowing in a Hele-Shaw cell at low Ca. The width of the cell is $W=6$, the viscosity contrast is $M=200$ and the dimensionless time is $t=7$. **a**, Initial condition; **b**, Ca=0.0001; **c**, Ca=0.001; **d**, Ca=0.005; and **e**, Ca=0.01.
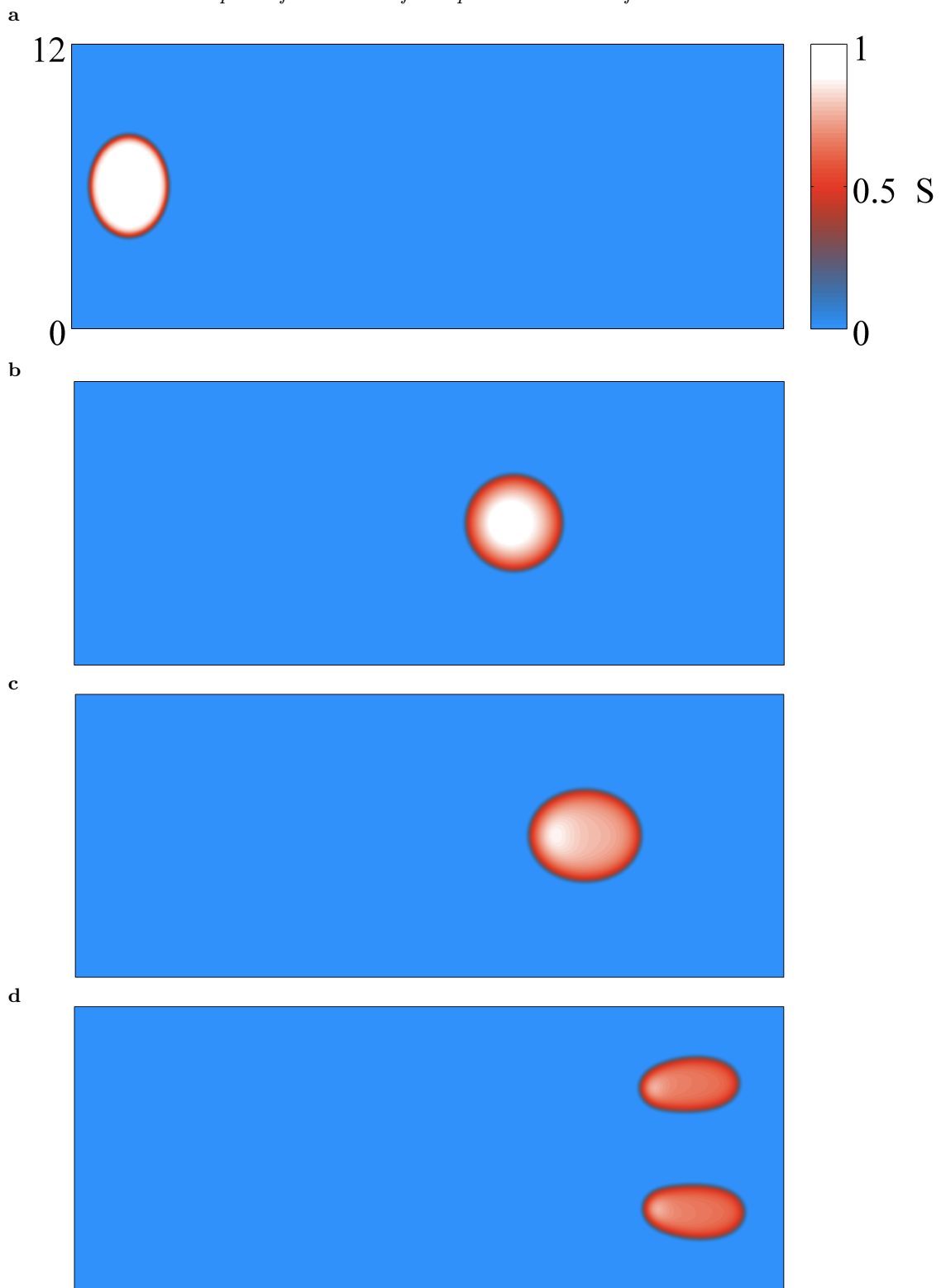
FIGURE 13. Two-dimensional simulations of bubbles flowing in a Hele-Shaw cell at low Ca. The width of the cell is $W=12$, the viscosity contrast is $M=200$ and the dimensionless time is $t=7$. **a**, Initial condition; **b**, Ca=0.0001; **c**, Ca=0.001; and **d**, Ca=0.01.
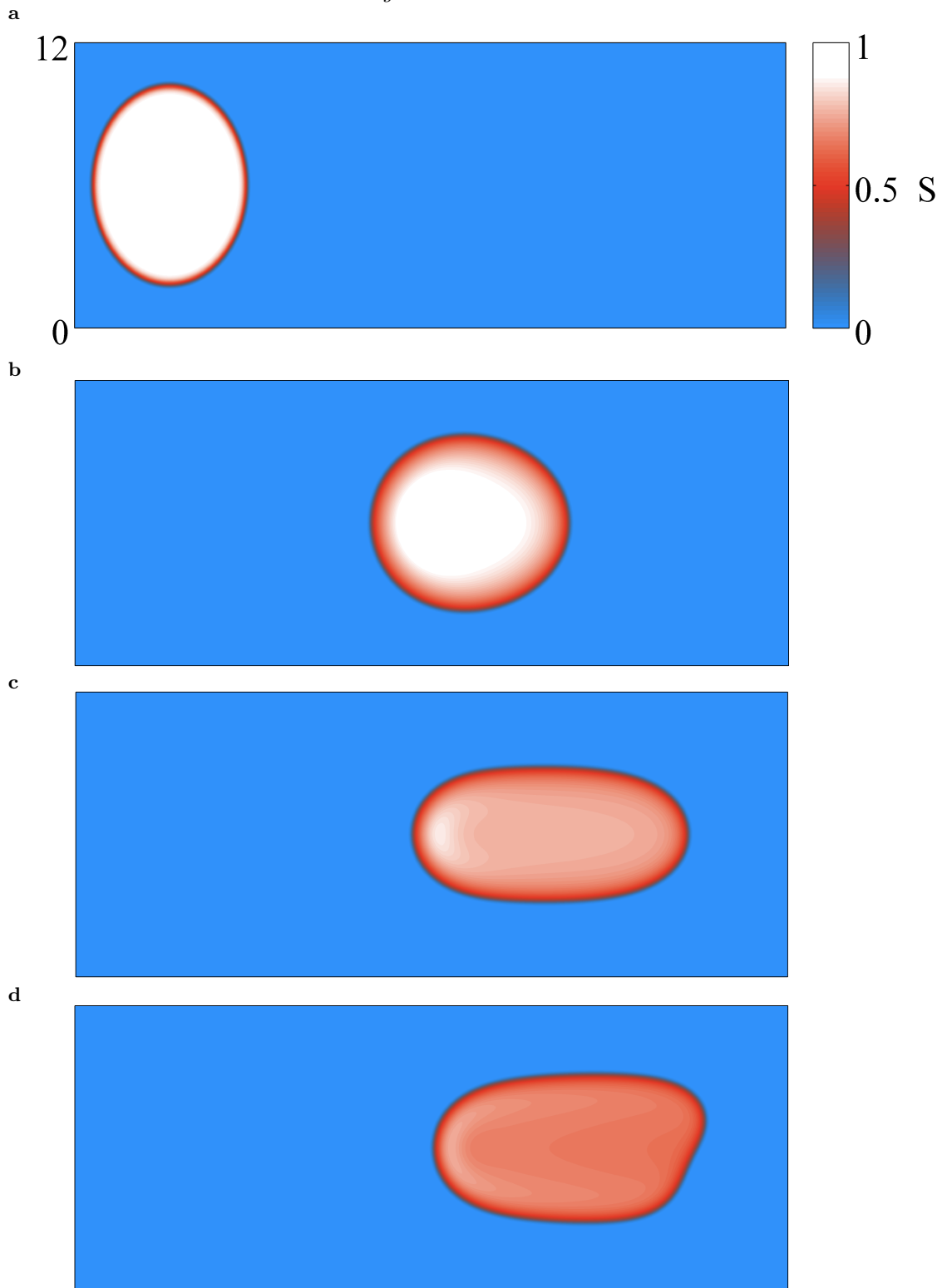
FIGURE 14. Two-dimensional simulations of bubbles flowing in a Hele-Shaw cell at low Ca. The width of the cell is $W=12$, the viscosity contrast is $M=200$ and the dimensionless time is $t=7$. **a**, Initial condition; **b**, Ca=0.0001; **c**, Ca=0.001; and **d**, Ca=0.005.
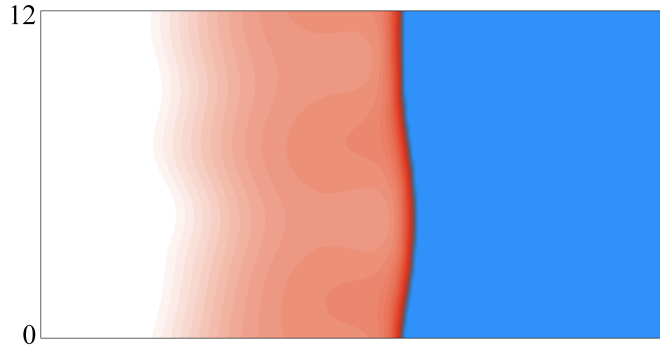
FIGURE 15. Two-dimensional simulation of constant flow rate, two-phase displacements in Hele-Shaw cells. For viscosity-matched fluids, the displacement front is stable. Here we show the saturation field for capillary number Ca=0.01. The initial perturbations in the fluid-fluid interface decay in time, and the interface is stable.

b

c

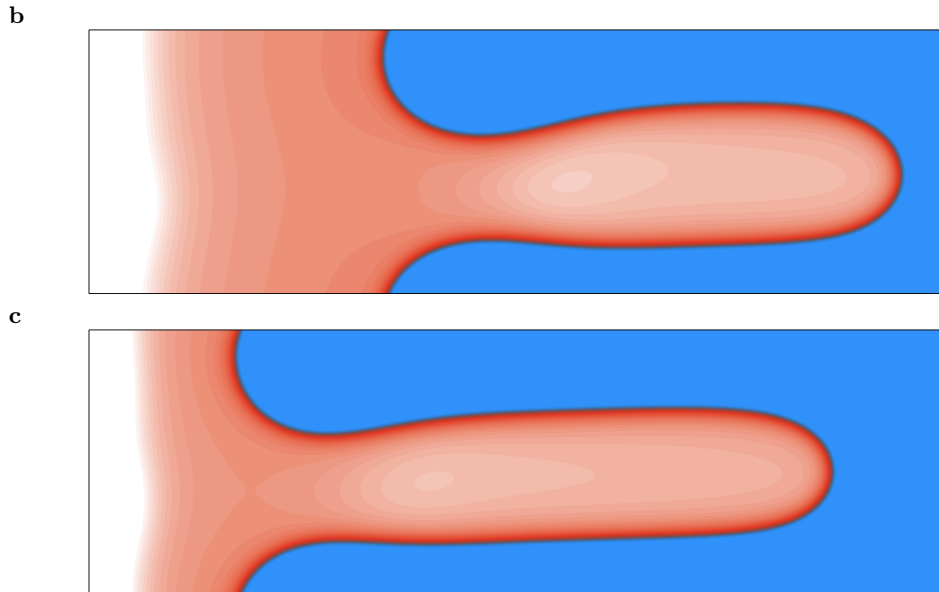FIGURE 16. Unstable displacement in a Hele-Shaw cell: the Saffman-Taylor finger. For two cases of unfavorable viscosity contrast—**a**, M=20, and **b**, M=500—and low capillary number, Ca=0.001, the displacement front evolves into a single finger that occupies roughly one half of the cell width, W=12.
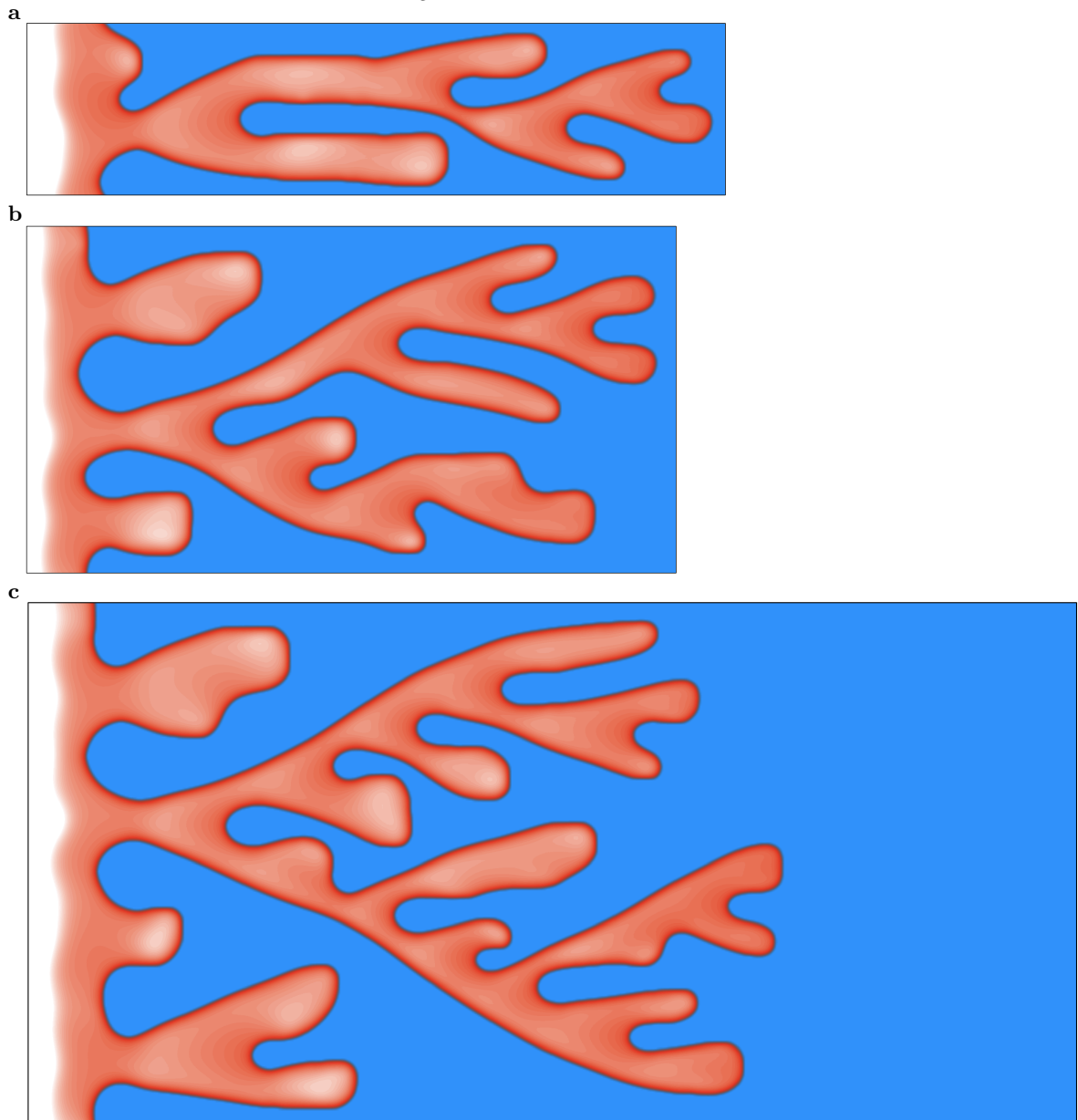
a

b

c

FIGURE 17. Two-dimensional simulation of constant flow rate, two-phase displacements in Hele-Shaw cells. When the invading fluid is less viscous than the defending fluid, the displacement front is unstable. Here, we show the saturation fields for constant-flux injection of gas with viscosity ratio $M=500$, and Ca=0.01. Varying the cell width, W, we investigate the impact of confinement on the displacement pattern. **a**, For $W=12$, the formation of fingers is constrained by the presence of the no-flow boundaries, implying relatively thick fingers. The finger size decreases as the boundary effect is eliminated with wider cells (**b**, $W=24$ and **c**, $W=36$. See Supplementary Movie 1).
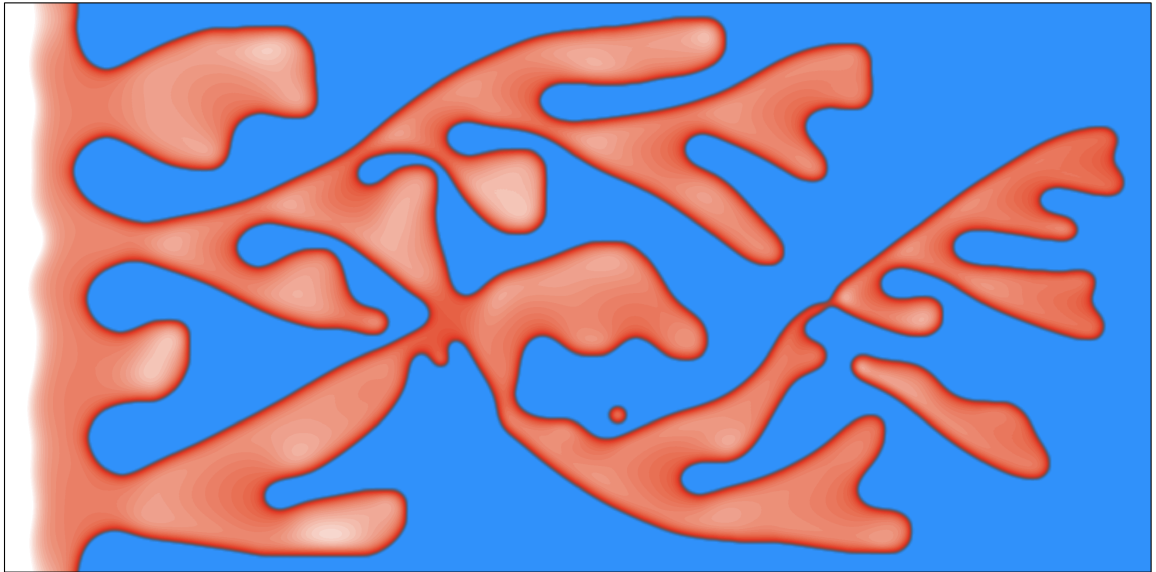
FIGURE 18. Pinchoff and reconnection in unstable displacements at large Ca and M. Here we show a snapshot of the simulation for M=500 and Ca=0.01 (Fig. 17**c**) at late times. The interaction between fingers results in pinch off and reconnection of fingers, and isolated bubbles that arise due to Rayleigh-Plateau instabilities (see Supplementary Movie 1).

REFERENCES

Al-Housseiny, T. T., Tsai, P. A. & Stone, H. A. 2012 Control of interfacial instabilities using flow geometry. *Nature Physics* **8**, 747–750.

Almgren, R., Dai, W.-S. & Hakim, V. 1993 Scaling behavior in anisotropic Hele-Shaw flow. *Phys. Rev. Lett.* **71**, 3461–3464.

Alvarez-Lacalle, E., Ortín, J. & Casademunt, J. 2004*a* Low viscosity contrast fingering in a rotating Hele-Shaw cell. *Phys. Fluids* **16**, 908–924.

Alvarez-Lacalle, E., Ortín, J. & Casademunt, J. 2004*b* Nonlinear Saffman-Taylor instability. *Phys. Rev. Lett.* **92**, 054501.

Alvarez-Lacalle, E., Ortín, J. & Casademunt, J. 2006 Relevance of dynamic wetting in viscous fingering patterns. *Phys. Rev. E* **74**, 025302.

Anderson, D. M., McFadden, G. B. & Wheeler, A. A. 1998 Diffuse-interface methods in fluid mechanics. *Annu. Rev. Mater. Res.* **30**, 139–165.

Anjos, P. H. A. & Miranda, J. A. 2013 Radial viscous fingering: Wetting film effects on pattern-forming mechanisms. *Phys. Rev. E* **88**, 053003.

Antanovskii, L. K. 1995 A phase-field model of capillarity. *Phys. Fluids* **7**, 747–753.

Arnéodo, A., Couder, Y., Grasseau, G., Hakim, V. & Rabaud, M. 1989 Uncovering the analytical Saffman-Taylor finger in unstable viscous fingering and diffusion-limited aggregation. *Phys. Rev. Lett.* **63**, 984–987.

Badalassi, V. E., Ceniceros, H. D. & Banerjee, S. 2003 Computation of multiphase systems with phase field models. *J. Comput. Phys.* **190**, 371–397.

Banpurkar, A. G., Limaye, A. V. & Ogale, S. B. 2000 Occurrence of coexisting dendrite morphologies: Immiscible fluid displacement in an anisotropic radial Hele-Shaw cell under a high flow rate regime. *Phys. Rev. E* **61**, 5507–5511.

Baroud, C. N., Gallaire, F. & Dangla, R. 2010 Dynamics of microfluidic droplets. *Lab Chip* **10**, 2032–2045.

Bear, J. 1972 *Dynamics of Fluids in Porous Media*. Wiley.

Ben-Jacob, E., Deitscher, G., Garik, P., Goldenfeld, N. G. & Lareah, Y. 1986 Formation of a dense branching morphology in interfacial growth. *Phys. Rev. Lett.* **57**, 1903–1906.

Ben-Jacob, E. & Garik, P. 1990 The formation of patterns in non-equilibrium growth. *Nature* **343**, 923–930.

Bensimon, D., Kadanoff, L. P., Liang, S., Shraiman, B. I. & Tang, C. 1986 Viscous flow in two dimensions. *Rev. Mod. Phys.* **58**, 977–999.

Benzi, R., Sbragaglia, M., Bernaschi, M. & Succi, S. 2011 Phase-field model of long-time glasslike relaxation in binary fluid mixtures. *Phys. Rev. Lett.* **106**, 164501.

Bertozzi, A. L., Ju, N. & Lu, H.-W. 2011 A biharmonic-modified forward time stepping method for fourth order nonlinear diffusion equations. *Discrete Cont. Dyn. S.* **29**, 1367–1391.

Bertozzi, A. L., Münch, A., Fanton, X. & Cazabat, A. M. 1998 Contact line stability and "undercompressive shocks" in driven thin film flow. *Phys. Rev. Lett.* **81**, 5169–5172.

Bertozzi, A. L., Münch, A. & Shearer, M. 1999 Undercompressive shocks in thin film flows. *Physica D* **134**, 431–464.

Bertozzi, A. L. & Shearer, M. 2000 Existence of undercompressive traveling waves in thin film equations. *SIAM J. Math. Anal.* **32**, 194–213.

Boyer, F. 2002 A theoretical and numerical model for the study of incompressible mixture flows. *Comput. Fluids* **31**, 41–68.

Bretherton, F. P. 1961 The motion of long bubbles in tubes. *J. Fluid Mech.* **10**, 166–188.

Buka, A., Kertész, J. & Vicsek, T. 1986 Transitions of viscous fingering patterns in nematic liquid crystals. *Nature* **323**, 424–425.

Buka, A., Palffy-Muhoray, P. & Rcz, Z. 1987 Viscous fingering in liquid crystals. *Phys. Rev. A* **36**, 3984–3989.

Cahn, J. W. 1961 On spinodal decomposition. *Acta Met.* **9**, 795–801.

Cahn, J. W. & Hilliard, J. E. 1958 Free energy of a nonuniform system. I. interfacial free energy. *J. Chem. Phys.* **28**, 258–267.

Carrillo, Ll., Magdaleno, F. X., Casademunt, J. & Ortin, J. 1996 Experiments in a rotating Hele-Shaw cell. *Phys. Rev. E* **54**, 6260–6267.

CARRILLO, LL., SORIANO, J. & ORTÍN, J. 1999 Radial displacement of a fluid annulus in a rotating Hele-Shaw cell. *Phys. Fluids* **11**, 778–785.

CARRILLO, LL., SORIANO, J. & ORTÍN, J. 2000 Interfacial instabilities of a fluid annulus in a rotating Hele-Shaw cell. *Phys. Fluids* **12**, 1685–1698.

CASADEMUNT, J. 2004 Viscous fingering as a paradigm of interfacial pattern formation: Recent results and new challenges. *Chaos* **14**, 809–824.

CASADEMUNT, J. & JASNOW, D. 1991 Defect dynamics in viscous fingering. *Phys. Rev. Lett.* **67**, 3677–3680.

CASADEMUNT, J. & MAGDALENO, F. X. 2000 Dynamics and selection of fingering patterns. Recent developments in the Saffman-Taylor problem. *Physics Reports* **337**, 1–35.

CENICEROS, H. D. & VILLALOBOS, J. M. 2002 Topological reconfiguration in expanding Hele-Shaw flow. *J. Turbul.* **3**, N37.

CHEN, C.-Y., HUANG, Y.-S. & MIRANDA, J. A. 2011 Diffuse-interface approach to Hele-Shaw flows. *Phys. Rev. E* **84**, 046302.

COMBESCOT, R., DOMBRE, T., HAKIM, V., POMEAU, Y. & PUMIR, A. 1986 Shape selection of Saffman-Taylor fingers. *Phys. Rev. Lett.* **56**, 2036–2039.

CORVERA-POIRÉ, E. & AMAR, M. BEN 1998 Finger behavior of a shear thinning fluid in a Hele-Shaw cell. *Phys. Rev. Lett.* **81**, 2048–2051.

CUETO-FELGUEROSO, L. & JUANES, R. 2008 Nonlocal interface dynamics and pattern formation in gravity-driven unsaturated flow through porous media. *Phys. Rev. Lett.* **101**, 244504.

CUETO-FELGUEROSO, L. & JUANES, R. 2012 Macroscopic Phase-Field Model of Partial Wetting: Bubbles in a Capillary Tube. *Phys. Rev. Lett.* **108**, 144502.

DANGLA, R., LEE, S. & BAROUD, C. N. 2011 Trapping Microfluidic Drops in Wells of Surface Energy. *Phys. Rev. Lett.* **107**, 124501.

DE GENNES, P. G. 1980 Dynamics of fluctuations and spinodal decomposition in polymer blends. *J. Chem. Phys.* **72**, 4756–4763.

DECKER, E. L., IGNÉS-MULLOL, J. & MAHER, J. V. 1999 Effect of lattice defects on Hele-Shaw flow over an etched lattice. *Phys. Rev. E* **60**, 1767–1774.

DEGREGORIA, A. J. & SCHWARTZ, L. W. 1986 A boundary-integral method for two-phase displacement in Hele-Shaw cells. *J. Fluid Mech.* **164**, 383–400.

DIAS, E. O. & MIRANDA, J. A. 2013 Wavelength selection in Hele-Shaw flows: A maximum-amplitude criterion. *Phys. Rev. E* **88**, 013016.

DING, H., SPELT, P. D. M. & SHU, C. 2007 Diffuse interface model for incompressible two-phase flows with large density ratios. *J. Comput. Phys.* **226**, 2078–2095.

DUIJN, C. J. VAN, PELETIER, L. A. & POP, I. S. 2007 A new class of entropy solutions of the Buckley-Leverett equation. *SIAM J. Math. Anal.* **39**, 507–536.

E, W. & PALFFY-MUHORAY, P. 1997 Phase separation in incompressible systems. *Phys. Rev. E* **55**, R3844.

ECK, W. & SIEKMANN, J. 1978 On Bubble Motion in Hele-Shaw Cell, a Possibility to Study Two-Phase Flows under Reduced Gravity. *Ing. Arch.* **47**, 153–168.

EMMERICH, H. 2008 Advances of and by phase-field modelling in condensed-matter physics. *Adv. Phys.* **57**, 1–87.

FAN, Y. & POP, I. S. 2011 A class of pseudo-parabolic equations: existence, uniqueness of weak solutions, and error estimates for the Euler-implicit discretization. *Math. Methods Appl. Sci.* **34**, 2329–2339.

FAST, P., KONDIC, L., SHELLEY, M. J. & PALFFY-MUHORAY, P. 2001 Pattern formation in non-Newtonian Hele-Shaw flow. *Phys. Fluids* **13**, 1191–1212.

FAST, P. & SHELLEY, M. J. 2004 A moving overset grid method for interface dynamics applied to non-Newtonian Hele-Shaw flow. *J. Comput. Phys.* **195**, 117–142.

FOLCH, R., CASADEMUNT, J., HERNÁNDEZ-MACHADO, A. & RAMIREZ-PISCINA, L. 1999*a* Phase-field models for Hele-Shaw flows with arbitrary viscosity contrast. I. theoretical approach. *Phys. Rev. E* **60**, 1724–1733.

FOLCH, R., CASADEMUNT, J., HERNÁNDEZ-MACHADO, A. & RAMIREZ-PISCINA, L. 1999*b* Phase-field models for Hele-Shaw flows with arbitrary viscosity contrast. II. numerical study. *Phys. Rev. E* **60**, 1734–1740.

FOURAR, M. & LENORMAND, R. 1998 A Viscous Coupling Model for Relative Permeabilities in Fractures. *SPE Paper 49006* .

GLASNER, K. 2003 A diffuse-interface approach to Hele-Shaw flow. *Nonlinearity* **16**, 49–66.

GLASS, R. J., RAJARAM, H., NICHOLL, M. J. & DETWILER, R. L. 2001 The interaction of two fluid phases in fractured media. *Current Opinion Colloid Interf. Sci.* **6**, 223–235.

GURTIN, M. E. 1994 Generalized Ginzburg-Landau and Cahn-Hilliard equations based on a microforce balance. *Physica D* **92**, 178–192.

HASSANIZADEH, S. M. & GRAY, W. G. 1993 Thermodynamic basis of capillary pressure in porous media. *Water Resour. Res.* **29**, 3389–3405.

HERNÁNDEZ-MACHADO, A., LACASTA, M., MAYORAL, E. & CORVERA-POIRÉ, E. 2003 Phase-field model of Hele-Shaw flows in the high-viscosity contrast regime. *Phys. Rev. E* **68**, 046310.

HOMSY, G. M. 1987 Viscous fingering in porous media. *Ann. Rev. Fluid Mech.* **19**, 271–311.

HONDA, T., HONJO, H. & KATSURAGI, H. 2006 Exprimental study on the morphology in a large Hele-Shaw cell. *J. Phys. Soc. Jpn.* **75**, 034005.

HOU, T. Y., LI, Z., OSHER, S. & ZHAO, H. 1997 A hybrid method for moving interface problems with application to the Hele-Shaw flow. *J. Comput. Phys.* **134**, 236–252.

HOU, T. Y., LOWENGRUB, J. S. & SHELLEY, M. J. 1994 Removing the stiffness from interfacial flows with surface tension. *J. Comput. Phys.* **114**, 312–338.

HOU, T. Y., LOWENGRUB, J. S. & SHELLEY, M. J. 2001 Boundary integral methods for multicomponent fluids and multiphase materials. *J. Comput. Phys.* **169**, 302–362.

HOWISON, S. D. 1986 Fingering in Hele-Shaw cells. *J. Fluid Mech.* **167**, 439–453.

JACQMIN, D. 1999 Calculation of two-phase Navier-Stokes flows using phase-field modeling. *J. Comput. Phys.* **155**, 96–127.

JASNOW, D. & VIÑALS, J. 1996 Coarse-grained description of thermo-capillary flow. *Phys. Fluids* **8**, 660–669.

KAWAGUCHI, M., HIBINO, Y. & KATO, T. 2001 Anisotropy effects of Hele-Shaw cells on viscous fingering instability in dilute polymer solutions. *Phys. Rev. E* **64**, 051806.

KAWAGUCHI, M., SHIMOMOTO, K., SHIBATA, A. & KATO, T. 1999 Effect of anisotropy on viscous fingering patterns of polymer solutions in linear Hele-Shaw cells. *Chaos* **9**, 323–328.

KAWAGUCHI, M., YAMAZAKI, S., YONEKURA, K. & KATO, T. 2004 Viscous fingering instabilities in an oil in water emulsion. *Phys. Fluids* **16**, 1908–1914.

KIM, J. 2005 A continuous surface tension force formulation for diffuse-interface models. *J. Comput. Phys.* **204**, 784–804.

KONDIC, L., PALFFY-MUHORAY, P. & SHELLEY, M. J. 1996 Models of non-Newtonian Hele-Shaw flow. *Phys. Rev. E* **54**, R4536.

KONDIC, L., PALFFY-MUHORAY, P. & SHELLEY, M. J. 1998 Non-Newtonian Hele-Shaw flow and the Saffman-Taylor instability. *Phys. Rev. Lett.* **80**, 1433–1436.

KOPF-SILL, A. R. & HOMSY, G. M. 1988*a* Bubble motion in a Hele-Shaw cell. *Phys. Fluids* **31**, 18–26.

KOPF-SILL, A. R. & HOMSY, G. M. 1988*b* Nonlinear unstable viscous fingers in Hele-Shaw flows. I. experiments. *Phys. Fluids* **31**, 242–249.

LAJEUNESSE, E. & COUDER, Y. 2000 On the tip-splitting instability of viscous fingers. *J. Fluid Mech.* **419**, 125–149.

LAMORGUESE, A. G. & MAURI, R. 2008 Diffuse-interface modeling of phase segregation in liquid mixtures. *Int. J. Multiph. Flow* **34**, 987–995.

LAX, P. D. 1957 Hyperbolic Systems of Conservation Laws II. *Comm. Pure Appl. Math.* **10**, 537–566.

LEE, H.-G, LOWENGRUB, J. S. & GOODMAN, J. 2002*a* Modeling pinchoff and reconnection in a Hele-Shaw cell. I. the models and their calibration. *Phys. Fluids* **14**, 492–513.

LEE, H.-G, LOWENGRUB, J. S. & GOODMAN, J. 2002*b* Modeling pinchoff and reconnection in a Hele-Shaw cell. II. analysis and simulation in the nonlinear regime. *Phys. Fluids* **14**, 514–545.

LEMAIRE, E., LEVITZ, P., DACCORDS, G. & DAMME, H. VAN 1991 From viscous fingering to viscoelastic fracturing in colloidal fluids. *Phys. Rev. Lett.* **67**, 2009–2012.

LI, S., LOWENGRUB, J. S., FONTANA, J. & PALFFY-MUHORAY, P. 2009 Control of viscous fingering patterns in a radial Hele-Shaw cell. *Phys. Rev. Lett.* **102**, 174501.

Li, S., Lowengrub, J. S. & Leo, P. H. 2007 A rescaling scheme with application to the long-time simulation of viscous fingering in a Hele-Shaw cell. *J. Comput. Phys.* **225**, 554–567.

Lindner, A., Bonn, D., Corvera-Poiré, E., Amar, M. Ben & Meunier, J. 2002 Viscous fingering in non-Newtonian fluids. *J. Fluid Mech.* **469**, 237–256.

Lindner, A., Bonn, D. & Meunier, J. 2000a Viscous fingering in a shear-thinning fluid. *Phys. Fluids* **12**, 256–261.

Lindner, A., Coussot, P. & Bonn, D. 2000b Viscous fingering in a yield stress fluid. *Phys. Rev. Lett.* **85**, 314–317.

Lowengrub, J. S. & Truskinovsky, L. 1998 Quasi-incompressible Cahn-Hilliard fluids and topological transitions. *Proc. R. Soc. A* **454**, 2617–2654.

Lu, H.-W., Glasner, K., Bertozzi, A. L. & Kim, C.-J. 2007 A diffuse-interface model for electrowetting drops in a Hele-Shaw cell. *J. Fluid Mech.* **590**, 411–435.

Maher, J. V. 1985 Development of viscous fingering patterns. *Phys. Rev. Lett.* **54**, 1498–1501.

Maruvada, S. R. & Park, C. W. 1996 Retarded motion of bubbles in Hele-Shaw cells. *Phys. Fluids* **8**, 3229–3233.

Maxworthy, T. 1986 Bubble formation, motion and interaction in a Hele-Shaw cell. *J. Fluid Mech.* **173**, 95–114.

McCloud, K. V. & Maher, J. V. 1995a Experimental perturbations to Hele-Shaw flow. *Physics Reports* **260**, 139–185.

McCloud, K. V. & Maher, J. V. 1995b Pattern selection in an anisotropic Hele-Shaw cell. *Phys. Rev. E* **51**, 1184–1190.

McLean, J. W. & Saffman, P. G. 1981 The effect of surface tension on the shape of fingers in a Hele-Shaw cell. *J. Fluid Mech.* **102**, 455–469.

Meiburg, E. 1989 Bubbles in a Hele-Shaw cell: numerical simulation and three-dimensional effects. *Phys. Fluids A* **1**, 938–946.

Meiburg, E. & Homsy, G. M. 1988 Nonlinear unstable viscous fingers in Hele-Shaw flows. II. numerical simulation. *Phys. Fluids* **31**, 429–439.

Miranda, J. A. & Alvarez-Lacalle, E. 2005 Viscosity contrast effects on fingering formation in rotating Hele-Shaw flows. *Phys. Rev. E* **72**, 026306.

Moore, M. G., Juel, A., Burgess, J. M., McCormick, W. D. & Swinney, H. L. 2002 Fluctuations in viscous fingering. *Phys. Rev. E* **65**, 030601(R).

Nagatsu, Y., Matsuda, K., Kato, Y. & Tada, Y. 2007 Experimental study on miscible viscous fingering involving viscosity changes induced by variations in chemical species concentrations due to chemical reactions. *J. Fluid Mech.* **571**, 475–493.

Nagel, M. & Gallaire, F. 2013 A new prediction of wavelength selection in radial viscous fingering involving normal and tangential stresses. *Phys. Fluids* **25**, 124107.

Nguyen, S., Folch, R., Verma, V. K., Henry, H. & Plapp, M. 2010 Phase-field simulations of viscous fingering in shear-thinning fluids. *Phys. Fluids* **22**, 103102.

Otto, F. & E, W. 1997 Thermodynamically driven incompressible fluid mixtures. *J. Chem. Phys.* **107**, 10177–10184.

Park, C.-W, Gorell, S. & Homsy, G. M. 1984 Two-phase displacement in Hele-Shaw cells: experiments. *J. Fluid Mech.* **141**, 257–287.

Park, C.-W & Homsy, G. M. 1984 Two-phase displacement in Hele-Shaw cells: theory. *J. Fluid Mech.* **139**, 291–308.

Park, C. W. & Homsy, G. M. 1985 The instability of long fingers in Hele-Shaw flows. *Phys. Fluids* **28**, 1583–1585.

Park, S. S. & Durian, D. J. 1994 Viscous and elastic fingering instabilities in foam. *Phys. Rev. Lett.* **72**, 3347–3350.

Paterson, L. 1981 Radial fingering in a Hele-Shaw cell. *J. Fluid Mech.* **113**, 513–529.

Persoff, P. & Pruess, K. 1995 Two-phase flow visualization and relative permeability measurement in natural rough-walled rock fractures. *Water Resour. Res.* **31**, 1175–1186.

Saffman, P. G. & Taylor, G. 1958a The penetration of a fluid into a porous medium or Hele-Shaw cell containing a more viscous liquid. *Proc. R. Soc. A* **245**, 312–329.

Saffman, P. G. & Taylor, G. I. 1958b The penetration of a fluid into a porous medium or Hele-Shaw cell containing a more viscous liquid. *Proc. R. Soc. Lond. A* **245**, 312–329.

Sarkar, S. K. 1990 Scaling dynamics of immiscible radial viscous fingering. *Phys. Rev. Lett.* **65**, 2680–2683.

SARKAR, S. K. & JASNOW, D. 1989 Viscous fingering in an anisotropic Hele-Shaw cell. *Phys. Rev. A* **39**, 5299–5307.

SHELLEY, M., TIAN, F.-R. & WLODARSKI, K. 1997 Hele-Shaw flow and pattern formation in a time-dependent gap. *Nonlinearity* **10**, 1471–1495.

SIEGEL, M. & TANVEER, S. 1996 Singular perturbation of smoothly evolving Hele-Shaw solutions. *Phys. Rev. Lett.* **76**, 419–422.

SIEGEL, M., TANVEER, S. & DAI, W.-S. 1996 Singular effects of surface tension in evolving Hele-Shaw flows. *J. Fluid Mech.* **323**, 201–236.

SOMFAI, E., SANDER, L. M. & BALL, R. C. 1999 Scaling and crossovers in Diffusion-Limited Aggregation. *Phys. Rev. Lett.* **83**, 5523–5526.

STRAIT, M., SHEARER, M., LEVY, R., CUETO-FELGUEROSO, L. & JUANES, R. 2013 Two Fluid Flow in a Capillary Tube. *submitted* .

SUN, Y. & BECKERMANN, C. 2004 Diffuse interface modeling of two-phase flows based on averaging: mass and momentum equations. *Physica D* **198**, 281–308.

SUN, Y. & BECKERMANN, C. 2007 Sharp interface tracking using the phase-field equation. *J. Comput. Phys.* **220**, 626–653.

SUN, Y. & BECKERMANN, C. 2008 A two-phase diffuse-interface model for Hele-Shaw flows with large property contrasts. *Physica D* **237**, 3089–3098.

TABELING, P., ZOCCHI, G. & LIBCHABER, A. 1987 An experimental study of the Saffman-Taylor instability. *J. Fluid Mech.* **177**, 67–82.

TANVEER, S. 1986 The effect of surface tension on the shape of a Hele-Shaw cell bubble. *Phys. Fluids* **29**, 3537–3548.

TANVEER, S. 2000 Surprises in viscous fingering. *J. Fluid Mech.* **409**, 273–308.

TRYGGVASON, G. & AREF, H. 1983 Numerical experiments on Hele-Shaw flow with a sharp interface. *J. Fluid Mech.* **136**, 1–30.

VLAD, D. H. & MAHER, J. V. 2000 Tip-splitting instabilities in the channel Saffman-Taylor flow of constant viscosity elastic fluids. *Phys. Rev. E* **61**, 5439–5444.

WEINSTEIN, S. J., DUSSAN, E. B. & UNGAR, L. H. 1990 A theoretical study of two-phase flow through a narrow gap with a moving contact line: viscous fingering in a Hele-Shaw cell. *J. Fluid Mech.* **221**, 53–76.

WHITAKER, N. 1994 Some numerical methods for the Hele-Shaw equations. *J. Comput. Phys.* **111**, 81–88.

WITELSKI, T. P. 1998 Equilibrium interface solutions of a degenerate singular Cahn–Hilliard equation. *Appl. Math. Lett.* **11**, 127–133.

YAMAMOTO, T., KAMIKAWA, H., TANAKA, H., NAKAMURA, K. & MORI, N. 2001 Viscous fingering of non-Newtonian fluids in a rectangular Hele-Shaw cell. *Nihon Reoroji Gakkaishi* **29**, 81–87.

YUE, P., FENG, J. J., LIU, C. & SHEN, J. 2004 A diffuse-interface method for simulating two-phase flows of complex fluids. *J. Fluid Mech.* **515**, 293–317.

ZHAO, H., CASADEMUNT, J., YEUNG, C. & MAHER, J. V. 1992 Perturbing Hele-Shaw flows with a small gap gradient. *Phys. Rev. A* **45**, 2455–2460.

ZHAO, H., CASADEMUNT, J., YEUNG, C. & MAHER, J. V. 1993 Erratum: Perturbing Hele-Shaw flows with a small gap gradient. *Phys. Rev. E* **48**, 1601.

ZHAO, H. & MAHER, J. V. 1993 Associating-polymer effects in a Hele-Shaw experiment. *Phys. Rev. E* **47**, 4278–4283.